Syn-convergent extension observed using the RETREAT GPS network, northern Apennines, Italy

R. A. Bennett,[1] E. Serpelloni,[2] S. Hreinsdóttir,[1] M. T. Brandon,[3] G. Buble,[1] T. Basic,[4,5] G. Casale,[6] A. Cavaliere,[2] M. Anzidei,[7] M. Marjonovic,[8] G. Minelli,[9] G. Molli,[10,11] and A. Montanari[12]

Received 8 August 2011; revised 25 January 2012; accepted 21 February 2012; published 21 April 2012.

[1] We present crustal deformation results from a geodetic experiment (Retreating-Trench, Extension, and Accretion Tectonics (RETREAT)) focused on the northern Apennines orogen in Italy. The experiment centers on 33 benchmarks measured with GPS annually or more frequently between 2003 and 2007, supplemented by data from an additional older set of 6 campaign observations from stations in northern Croatia, and 187 continuous GPS stations within and around northern Italy. In an attempt to achieve the best possible estimates for rates and their uncertainties, we estimate and filter common mode signals and noise components using the continuous stations and apply these corrections to the entire data set, including the more temporally limited campaign time series. The filtered coordinate time series data are used to estimate site velocity. We also estimate spatially variable seasonal site motions for stations with sufficient data. The RMS scatter of residual time series are generally near 1 mm and 4 mm, horizontal and vertical, respectively, for continuous and most of the new campaign stations, but scatter is slightly higher for some of the older campaign data. Velocity uncertainties are below 1 mm/yr for all but one of the stations. Maximum rates of site motion within the orogen exceed 3 mm/yr (directed NE) relative to stable Eurasia. This motion is accommodated by extension within the southwestern and central portions of the orogen, and shortening across the foreland thrust belt to the northeast of the range. The data set is consistent with contemporaneous extension and shortening at nearly equal rates. The northern Apennines block moves northeast faster than the Northern Adria microplate. Convergence between the Northern Apennines block and the Northern Adria microplate is accommodated across a narrow zone that coincides with the northeastern Apennines range front. Extension occurs directly above an intact vertically dipping slab inferred by previous authors from seismic tomography. The observed crustal deformation is consistent with a buried dislocation model for crustal faulting, but associations between crustal motion and seismically imaged mantle structure may also provide new insights on mantle dynamics.

Citation: Bennett, R. A., et al. (2012), Syn-convergent extension observed using the RETREAT GPS network, northern Apennines, Italy, *J. Geophys. Res.*, *117*, B04408, doi:10.1029/2011JB008744.

1. Introduction

[2] Late Cenozoic deformation of the northern Apennines, Italy, (Figure 1) has attracted scientific interest for decades, but community consensus regarding active deformation of the orogen, particularly regarding activity within the foreland thrust belt, has not yet emerged (Figure 2). The mountain chain is often described as a convergent orogenic wedge that has experienced orogen-perpendicular extension coeval with and in close proximity to the locus of crustal shortening and accretion. Several hypotheses have been

[1]Department of Geosciences, University of Arizona, Tucson, Arizona, USA.
[2]Istituto Nazionale di Geofisica e Vulcanologia, Sezione di Bologna, Bologna, Italy.
[3]Department of Geology and Geophysics, Yale University, New Haven, Connecticut, USA.
[4]Faculty of Geodesy, University of Zagreb, Croatian Geodetic Institute, Zagreb, Croatia.
[5]Croatian Geodetic Institute, Zagreb, Croatia.
[6]Department of Earth and Space Sciences, University of Washington, Seattle, Washington, USA.
[7]Istituto Nazionale di Geofisica e Vulcanologia, Centro Nazionale Terremoti, Rome, Italy.
[8]Croatian State Geodetic Administration, Zagreb, Croatia.
[9]Dipartimento di Scienze della Terra, Universitá di Perugia, Perugia, Italy.
[10]Dipartimento di Scienze della Terra, Universita` di Pisa, Pisa, Italy.
[11]Istituto di Geoscienze e Georisorse, CNR, Pisa, Italy.
[12]Osservatorio Geologico di Coldigioco, Frontale di Apiro, Italy.

0148-0227/12/2011JB008744

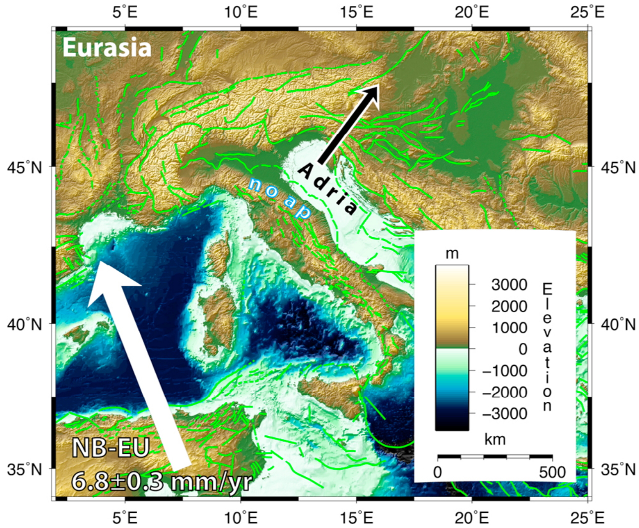

Figure 1. Tectonic setting of the central Mediterranean portion of the Nubia-Eurasia plate boundary zone. White vector shows MORVEL estimate for Nubia-Eurasia relative plate motion from *DeMets et al.* [2010]. The Adria region, which underlies the Adriatic Sea, behaves like a microplate, with motion (black vector) distinct from both Eurasia and Nubia. Green lines represent mapped faults from the Geodynamic Map of the Mediterranean project. Fault zones within and around the northern Apennines (noap) in northern Italy strike NW-SE, similar to the relative motion of the major plates. The northern Apennines are located in the interior of the plate boundary zone, such that they do not interact directly with the Nubia plate. Instead, deformation within the northern Apennines involves Adria-Eurasia relative motion (black vector), which is oriented at high angle to Nubia-Eurasia relative motion.

advanced to explain this unusual pairing of extension and shortening, with important implications for the geodynamic processes that characterize the closure of ocean basins, as well as assessments of contemporary hazards. Proposed hypotheses explaining the syn-convergent nature of the northern Apennines include (1) rollback of a negatively buoyant subducting slab causing extension of the overriding plate analogous to back arc spreading inboard of retreating oceanic subduction zones (Figure 2a) [*Malinverno and Ryan*, 1986; *Royden*, 1993; *Pialli and Alvarez*, 1995], (2) complete or partial detachment of an oceanic slab following collision with a buoyant continental passive margin (Figure 2b) [*Royden*, 1993; *Carminati et al.*, 1998; *Wortel and Spakman*, 2000; *Gvirtzman and Nur*, 2001; *Stein and Sella*, 2006], (3) upper plate retreat driven by resistance of subducted slabs to the net westward drift of the lithosphere relative to the mesosphere (Figure 2c) [*Doglioni*, 1990, 1991], and (4) late stage orogenic collapse, or gravitational collapse of an over thickened orogenic wedge (Figure 2d) [*Platt*, 1986; *Carmignani and Kligfield*, 1990; *Jolivet et al.*, 1998; *Argnani et al.*, 2003]. A cornerstone argument of the slab rollback interpretation for the northern Apennines (Figure 2a)—one of the most widely accepted of the interpretations for the Cenozoic history of the orogen—is the observation that Nubia-Eurasia relative motion occurred at high angle to the predominant direction of the crustal shortening underpinning the formation of the northern Apennines orogen (Figure 1); assuming that Adria was a promontory of Nubia for most of the early Cenozoic history [e.g., *Rosenbaum and Lister*, 2004], this observation implies that convergence across the Apennines fold and thrust belt was driven by some process other than Nubia-Eurasia relative plate motion.

[3] The proposed hypotheses for late Cenozoic crustal deformation imply different driving mechanisms for recent deformation. Some authors advocate ongoing coeval shortening and extension in association with present-day slab subduction and rollback [e.g., *Galadini and Messina*, 2004; *Picotti and Pazzaglia*, 2008; *Faccenda et al.*, 2009]. In contrast, other authors argue that subduction (and by implication shortening), ceased during the late Quaternary after the northern Apennines wedge overrode the thicker passive margin of the Adria continental platform during Pliocene time [e.g., *Royden*, 1993; *Wortel and Spakman*, 2000; *Di Bucci and Mazzoli*, 2002]. According to the former hypothesis, syn-convergent extension continues to characterize the present-day deformation field, whereas the latter hypothesis maintains that the system has undergone a more or less complete transition from a Mio-Pliocene phase of paired extension and shortening to a modern phase characterized predominantly by orogenic collapse or continental rifting with no ongoing subduction, shortening, or accretion [e.g., *Stein and Sella*, 2006]. Discriminating between these and other interpretations of the available geologic and geophysical data has proven difficult given that rates are small and difficult to resolve.

[4] To address this problem, we designed a campaign Global Positioning System (GPS) network across the northern Apennines orogen. We adopted existing, older monuments where available, and constructed new monuments to increase the density of the network. The goal of the project was to measure the pattern of present-day crustal deformation, providing new data with which to assess the contemporary strain rate field of the northern Apennines, contributing to our understanding of the modern geodynamic setting. The network was established in 2003 at a time of sparse prior campaign and continuous GPS (CGPS) station coverage within and around the orogen [e.g., *Serpelloni et al.*, 2005]. However, since the establishment of our new campaign network, a large number of continuous GPS (CGPS) networks were installed for both geodynamic and surveying engineering applications, providing valuable additional data with which to study the active deformation pattern. In this paper, we present crustal deformation results derived from the combined campaign and continuous GPS data set. We describe our analysis of the GPS data in detail, and present estimates for coordinate time series and site velocities relative to a Eurasia fixed reference frame. We use these kinematic results to investigate the pattern of present-day crustal deformation in and around the northern Apennines orogen. We speculate on the possible implications of the GPS velocity field for geodynamic models, reserving a detailed numerical assessment of deformation models for future work.

2. Active Tectonics Background

[5] The northern Apennines are bound to the northeast by a deformation front that is buried beneath the Po Valley and

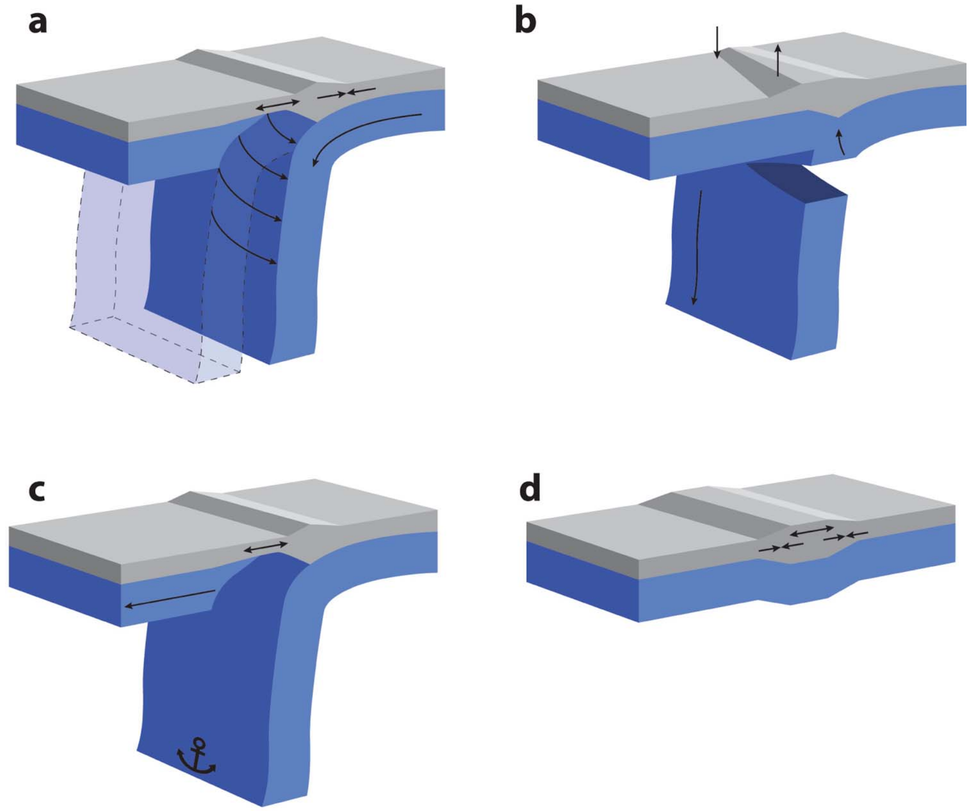

Figure 2. Proposed end-member models for the contemporary geodynamic setting of the northern Apennines from the literature. (a) Slab rollback drives upper plate extension within and behind the retro-wedge, as well as shortening and accretion in the pro-wedge. (b) Slab tear (or complete slab detachment) leads to isostatic uplift and extension of the orogen as asthenospheric mantle replaces dense lithospheric mantle over the detached slab. Subduction of intact portions of the slab at the leading edge of the tear may be enhanced due to increased slab pull. (c) Upper plate retreat due to drift of the lithosphere relative to the deeper mantle. The slab penetrates the deeper mantle and acts as a "drift anchor," resisting motion of the lower plate, which slows it relative to the upper plate. (d) Gravitational collapse of an overthickened orogen drives a symmetric pattern of shortening in the pro- and retro-wedges and extension in the orogen's interior.

extends offshore beneath the western Adriatic Sea. Reflection profiles indicate that folding and thrusting associated with this front are largely inactive at this time [*Picotti and Pazzaglia*, 2008]. The range front of the Apennines lies some 60 km to the southwest of the deformation front. The range front is marked by a transition from gently dipping strata of the Po basin, to uplifted bedrock of the Apennines, which now stand some 2000 m above the Po plain. *Benedetti et al.* [2003] and *Picotti and Pazzaglia* [2008] provide evidence from range front geomorphology, Po basin stratigraphy, and other data that the topography of the range front represents the forward dipping limb of an anticline overlying a blind steeply dipping reverse fault. We refer to these external and internal thrust belt features as the Apennine Deformation Front (ADF) and the Apennine Range Front (ARF), respectively (Figure 3).

[6] The Apennines are characterized by low-level seismicity, most of which is associated with normal faulting. Diffuse, small magnitude earthquakes are frequent in the northern Apennines (Figure 3), but larger earthquakes seldom exceed magnitude M5.5. No earthquake of magnitude greater than ~M6.5 has been recorded instrumentally or inferred from historic data [*Pondrelli et al.*, 2001]. The record of historic seismicity in the northern Apennines goes back to at least 1100 AD (cf., http://emidius.mi.ingv.it/CPTI08/). The four strongest historic earthquakes are each thought to be in the range of M6.0 to M6.5: the 1501 Apennino Modenese, 1542 Mugello, 1688 Romagna, and 1920 Garfagnana earthquakes [*Calderoni et al.*, 2009; *de Ferrari et al.*, 2010] (see also http://storing.ingv.it/cfti4med/). The 1920 event appears to have been tentatively associated with a mapped normal fault that bounds the Garfagnana basin. The 1501, 1542, and 1688 events are spatially associated with the ARF (Figure 3) [*Montone and Mariucci*, 1999], but the shear sense for these earthquakes is not known. More recent earthquakes from this region, such as the 1971 M_b 5.7, 1983 M_s 5.0 Parma [*Selvaggi et al.*, 2001], 1996 M_w 5.4 Reggio Emilia [*Selvaggi et al.*, 2001], and 2003 M_w 5.3 Monghidoro [*Piccinini et al.*, 2006], have thrust-sense focal plane solutions (Figure 3).

[7] Slip vectors from major earthquakes throughout the circum-Adriatic region, including the central and southern

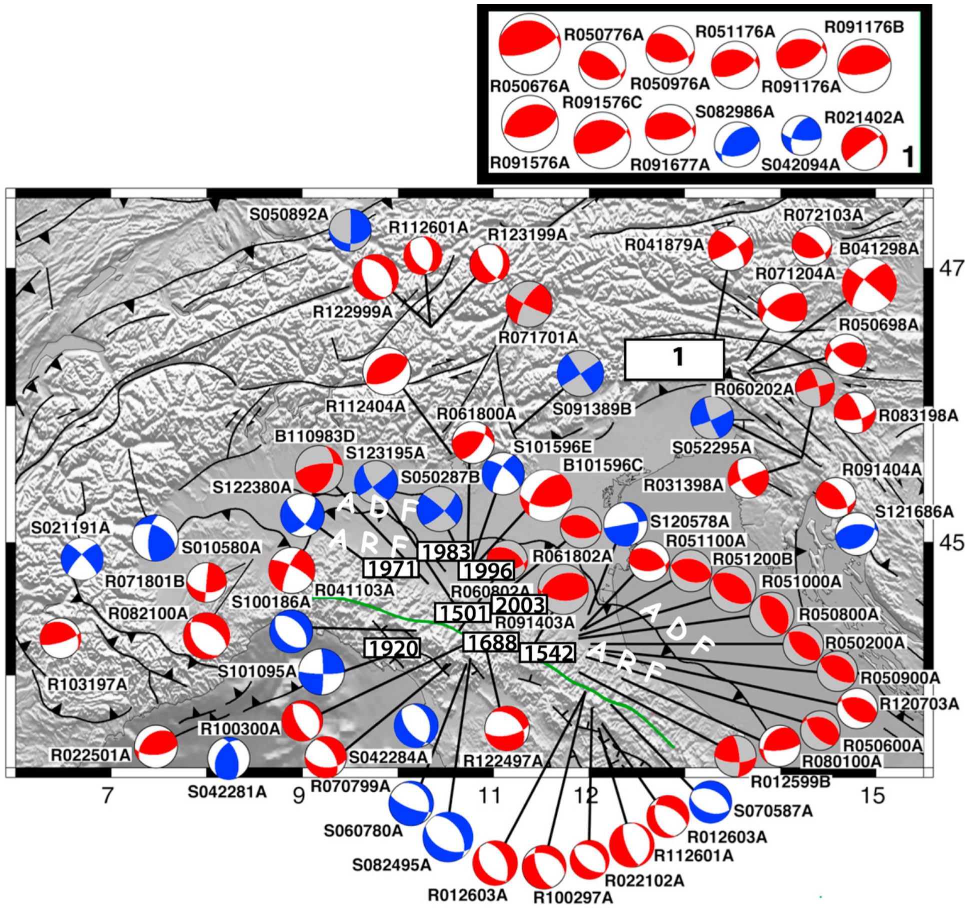

Figure 3. Focal mechanisms and seismicity pattern for instrumentally recorded earthquakes in the northern Apennines [after *Pondrelli et al.*, 2006]. Focal mechanism color indicates source of data from Harvard and INGV catalogs (red) or *Pondrelli et al.* [2006] (blue). Focal mechanisms with gray background indicate seismicity with focal depth greater than 20 km. ARF shows the general location of the Apennines Range Front. ADF shows the location of the Apennines Deformation Front. Seismicity in the hinterland of the northern Apennines orogen is characterized by normal fault mechanisms, whereas the foreland is characterized by thrust events. Dates in boxes indicate locations of specific earthquakes referenced in the text: 1501 Apennino Modenese, 1542 Mugello, 1688 Romagna, 1920 Garfagnana, 1971 Parma, 1983 Parma, 1996 Reggio Emilia, 2003 Monghidoro. There are no focal mechanisms shown for events prior to 1971. Large white box labeled 1 shows the location of the inset at top right.

Apennines and the External Dinarides in Croatia and Montenegro have been used to infer the overall style of active deformation characterizing the entire Apennines chain. *Anderson and Jackson* [1987], *D'Agostino et al.* [2008], and *Weber et al.* [2010] used slip vector azimuths of selected earthquakes within the Apennines and Dinarides orogens to infer pervasive extensional deformation within the Apennines along the entire length of the range, including the northern Apennines, in association with counterclockwise rotation of one or more Adria microplates relative to Eurasia. However, *Anderson and Jackson* [1987] used slip vectors from only one earthquake in the northern Apennines, and *Weber et al.* [2010] used only slip vectors from outside of the northern Apennines. These previous studies of northern Apennines kinematics based on focal mechanism data did not incorporate the smaller magnitude thrust earthquakes in the frontal belt of the northern Apennines, nor did they test the possibility of paired belts of active shortening and extension associated with the northern Apennines.

[8] One of the factors limiting our understanding of the active tectonic setting of the northern Apennines is that most earthquakes do not rupture the surface [*Galadini et al.*, 2001; *Galli et al.*, 2008]. This is particularly true of the outermost foreland thrusts, which are buried beneath a thick blanket of Plio-Quaternary sediments in the Po Plain. Seismic reflection data have been used to infer the timing of faulting associated with these Po Plain structures. These reflection data reveal relatively undisturbed Quaternary sediments, interpreted by some researchers as an indication that shortening has ceased [e.g., *Bertotti et al.*, 1997]. However, the absence of observable Quaternary deformation associated with the outermost ADF thrusts within the Po Plain has also been interpreted as an indication of backstepping of the active thrust front to the ARF [e.g., *Picotti and Pazzaglia*, 2008].

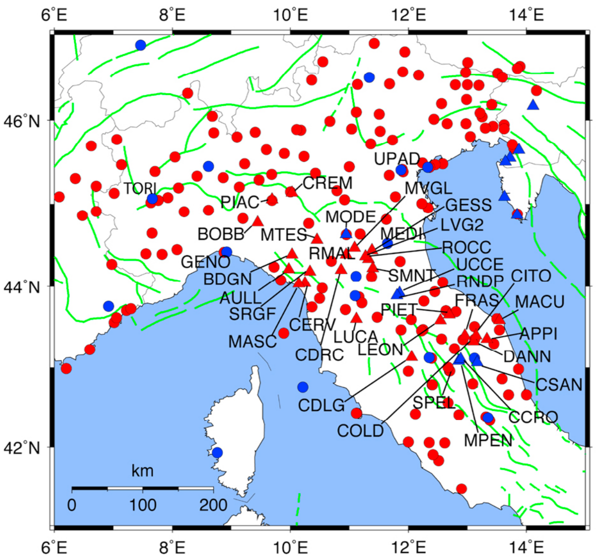

Figure 4. Distribution of GPS stations in northern Italy used in this study. In 2003, before we began our experiment, the number of campaign (blue triangles) and continuous (blue circles) GPS stations was severely limited. During the course of our experiment, numerous additional stations were installed throughout the area by ourselves and others. Red triangles represent campaign (or semi-continuous) GPS sites that were first surveyed during or after 2004. Red circles represent continuous GPS stations that began operation during or after 2004. Note that the majority of the new (red) continuous (circles) GPS stations added since 2004 are located primarily outside of the northern Apennines. The density of stations is greatly improved by the new (red) campaign sites (triangles). Site names are provided for the 33 stations that formed the core sub-network of our campaign/semi-continuous geodetic experiment, as well as for select older continuous GPS stations (GENO, MEDI, TORI, and UPAD), which are referred to in the text.

[9] Few geodetic studies have focused specifically on the northern Apennines. *Calais et al.* [2002] report GPS measurements of active deformation in the western Alps. They estimated the motion of the Adriatic plate, which subducted beneath the Apennines during Pliocene time, using four CGPS stations in northern Italy (GENO, MEDI, TORI, UPAD), all of which were located outboard of the modern Apennine deformation front (Figure 4). Their results were consistent with the kinematic analysis of *Anderson and Jackson* [1987], which predicted counterclockwise rotation of northern Adria with respect to a Eurasia-fixed reference frame. A more detailed image of northern Apennines deformation was obtained by *Serpelloni et al.* [2005, 2006], who analyzed a large set of campaign and continuous GPS data covering the central Mediterranean region (blue triangles and circles, respectively, in Figure 4). Serpelloni et al. provided the first synoptic view of Nubia-Eurasia plate boundary zone deformation in the central Mediterranean, demonstrating orogen-perpendicular extension along the entire Apennine range, as well as providing evidence for contemporary shortening within the external thrust belt of the northern Apennines. However, the rate and pattern of this shortening were poorly resolved due to the sparse network in northern Italy at the time of that study.

[10] The GPS data reported here provide a much better resolved image of contemporary crustal deformation. We focus mainly on estimation of site velocities and an assessment of velocity uncertainty. We briefly speculate on possible implications of these data for geodynamics, but reserve detailed geodynamic modeling of crustal kinematics for future work.

3. Description of Network

[11] We here report results for 226 campaign and continuous GPS stations, observed from the period 1996 to 2010 over an area that spans the northern Italian peninsula from the Adriatic Sea to the Tyrrhenian Sea in the latitude range of ~43.0°N to ~45.5°N (Figure 4). Our project started with campaign-style observation of 23 new monuments, and 10 existing benchmarks. Most stations are concentrated within the northern Apennines Mountains or over the Apennines' frontal fold and thrust belt buried beneath the Po Plain. Several stations (AULL, CERV, DANN, GESS, MASC, MACU, SRGF) were occupied semi-continuously, recording data for a few months per campaign during various years of the experiment. We ran two additional stations (COLD and SPEL) continuously for the period of 2004–2007. The 10 existing benchmarks that we adopted have a prior history of measurements, which are described by *Serpelloni et al.* [2005].

[12] Most of our new monuments consist of stainless-steel benchmarks [*Cavaliere et al.*, 2010] anchored 20 cm into either exposed rock outcrops or into meters-thick castle walls built directly on bedrock. (Six suboptimal monuments are discussed below.) Each of the new stainless-steel benchmarks was precisely leveled. Stainless-steel masts of various heights in the range of 10 to 25 cm were threaded into the benchmarks. Antennas were attached directly to these masts and oriented to true north. This benchmark-mast system provided sufficient long-term stability for continuous or semi-continuous deployments. Monumentation for the existing sites involve geodetic markers set on concrete pillars.

[13] Six of the new GPS stations are based on suboptimal monumentation on brick or wooden buildings, due to the absence of suitable outcrops or large stone castle structures. For one station (SPEL), we used a rod attached to the roof of a large building at the apex of a stone walled medieval hilltop city, presumably constructed on a stable rock foundation. This station was operated continuously for the majority of the experiment (mid-2005 to mid-2008), which allows us to precisely assess the short-term stability of the monument. The five additional exception sites involved installation of the leveled fixed-height stainless steel monuments on the roofs of buildings (APPI, COLD, DANN, MACU, MVGL). Site COLD was occupied continuously from mid-2004 to mid-2008 allowing us to assess its short-term stability. Five of the six suboptimal sites are fortuitously located within a region spanned by a new, dense network of continuous GPS stations operated by the Laboratorio di Topografia (LabTopo) University of Perugia (cf., http://labtopo.ing.unipg.it/labtopo/). This particular network was established for the purposes of surveying engineering applications, but has been shown in previous studies [e.g., *Hreinsdóttir*

and Bennett, 2009; *D'Agostino et al.*, 2009] to produce reliable data for tectonics applications.

[14] Those stations that were not operated continuously were surveyed using GPS, nominally once per year in the late Summer/early Fall [*Cavaliere et al.*, 2010]. Occupation campaigns typically lasted about five to seven days each. We made a concerted effort to conduct each campaign during the same season each year in order to mitigate the effects of seasonal site motion on our estimates for secular site velocity, as described in more detail below. Some stations were not installed until the second or third campaign, and a subset of stations were occupied again in 2008 following the main phase of our GPS experiment. For most measurements, we used Trimble Zephyr Geodetic antennas and either Trimble NetRS or Trimble R7 receivers borrowed from the UNAVCO Facility pool. Some data were collected by INGV personnel using either Leica GRX1200 series receivers with AX1202 antennas or Ashtech receivers with choke-ring antennas. Older campaign measurements were also collected with a variety of equipment types.

4. GPS Data Analysis

4.1. Analysis of Phase Data and Estimation of Coordinate Time Series

[15] We analyzed all of these campaign GPS data together with data from ~1500 continuous GPS (CGPS) stations, 187 of which are located within our northern Apennines study region (Figure 4). The remaining ~1300 stations are located throughout the Eurasian plate interior and globally and are not reported on here. This broad distribution of CGPS stations facilitated transformation between global and Eurasia-fixed reference frames, and allowed us to estimate precise adjustments to orbital and Earth orientation parameters (as described next).

[16] We analyzed all of the available data following standard methods using the GAMIT/GLOBK software version 10.3 [*Herring et al.*, 2010a, 2010b], which incorporates International GNSS Service (IGS) absolute phase center and ocean-loading (FES2004) models. We used precise IGS products for orbital parameters and Earth orientation parameters as a priori constraints, but we estimated corrections to these a priori estimates. In addition to estimating adjustments to Earth orientation and satellite-orbital parameters, we used GAMIT to estimate zenith tropospheric delay parameters, carrier-phase ambiguities, and adjustments to a priori station coordinates for each UTC day for which we had data. The GPS phase data errors were estimated during the GAMIT analyses using an elevation-angle dependent model through an iterative analysis procedure whereby the elevation dependence was determined from the observed scatter of phase residuals [*Herring et al.*, 2010a, 2010b].

[17] We then used GLOBK to determine the evolution of our site coordinate estimates through time by minimizing the net rotation and translation among the coordinate adjustments [*Dong et al.*, 1998], relative to the ITRF05-Eurasia reference frame [*Altamimi et al.*, 2007]. We obtained this Eurasia-fixed reference frame by rotating the global ITRF05 reference velocities to the Eurasia-fixed frame using the transformation parameters provided by *Altamimi et al.* [2007]. The weighted root-mean squared (WRMS) scatter among stations within the Eurasia plate interior is in the range ~0.3 to 0.6 mm/yr, depending on the set of stations selected. The small RMS indicates that the realized reference frame is consistent with very small rotation rate relative to this frame. Errors associated with the realization of a reference frame manifest primarily as common-mode motions across the network. Common-mode motions may take the form of rigid body translation, rotations, as well as seasonal variations of the entire network. When the number of stations available to define the reference frame is low, distortions of the network may also occur that mimic crustal strain [*Larson and Webb*, 1991]. However, the global reference frame for our analysis is based on a very large number (>100) of globally distributed stations so we assume that local distortions associated with reference frame error are negligible. Our analysis of the deformation field, presented below, is based primarily on velocity gradients and is thus only marginally dependent on the velocity reference frame as described in detail below.

4.2. Time Series Analysis and Assessment of Common-Mode Variations

[18] The coordinate time series for each station obtained from our GAMIT/GLOBK analysis represents the evolution of position for that site with respect to a Eurasia-fixed reference frame. Because the northern Apennines deformation signals that we seek to scrutinize are small (of order 1 mm/yr), we performed a detailed analysis of the coordinate time series in an attempt to form the most precise estimates possible, and develop an understanding of the uncertainties associated with the velocity data set as completely as possible.

[19] We accounted for potential common-mode reference frame errors by analyzing the kinematics of the site motions recorded by these coordinate time series in several steps. First, we estimated and removed a "Common-Mode Signal" (CMS) from the coordinate time series, assuming a Gaussian white noise error model. The model for CMS consists of a set of parameters for net-translational velocity and seasonal-site motion for annual and semi-annual periods, representing the trend and periodic motions averaged among all of the continuous sites. We estimated the parameters of the CMS using data from the continuous sites, but we reduced the coordinate time series for both continuous and campaign sites using the predicted displacements associated with the inferred CMS model. The slopes of the resulting Common-mode Signal Reduced (CSR) time series represent site motions associated with rigid-body rotation relative to the continuous GPS network centroid, as well as the deformational component of velocity representing strain accumulation within the network. CSR time series for four select stations are shown in Figure 5.

[20] We used the CSR time series to estimate secular velocities ("CSR velocities") and annual and semi-annual periodic motions at each site, component-by-component. The residual time series, which are obtained by subtracting the best fit kinematic models from the CSR time series, were then stacked and averaged to form an estimate for common-mode noise, similar to the procedure described by *Wdowinski et al.* [1997]. We subtracted this Common-mode Noise Process (CNP) from the residual time series forming a Final Filtered Residual (FFR) time series from which we assess

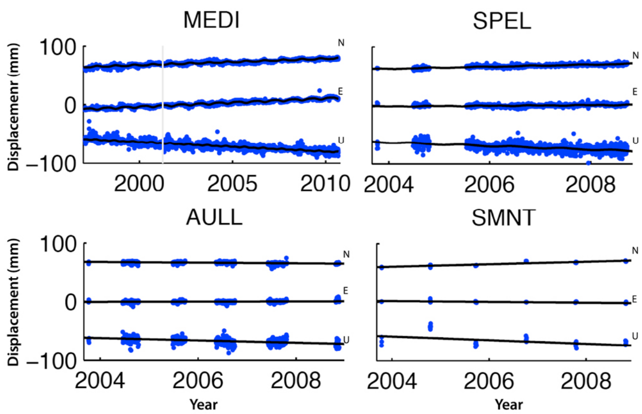

Figure 5. Representative time series for IGS site MEDI, continuous site SPELL, semi-continuous site AULL, and campaign site SMNT. The gray vertical line crossing the MEDI time series represents an epoch for which an antenna offset was estimated during the time series analysis.

measurement precision using standard root-mean square (RMS) statistics.

[21] Table 1 lists the CSR estimates for velocity and periodic terms, and RMS statistics associated with the residual-error time series. We note that the NRMS values, which represent misfit of the kinematic models to the coordinate times series are on average about 0.5 for the continuous stations (Table 1), indicating that the scaling of the phase data errors determined at the GAMIT stage of processing conservatively characterize the precision of the continuous coordinate time series data. NRMS values for the campaign stations are on average near unity. If we were to assume that the continuous coordinate time series data were uncorrelated with time, we would rescale the uncertainties in the kinematic parameters derived from the continuous time series by the NRMS value 0.5, which would *decrease* the formal uncertainties associated with the parameter estimates by a factor of two. However, we choose to forego this rescaling in an attempt to account (informally) for possible unmodeled temporal correlations within each coordinate time series. We do not expect that parameter estimates derived from the temporally sparse campaign time series data to be affected appreciably by temporal correlations. A more accurate analysis of the possible error processes contaminating the time series data would require an understanding of the power spectral density of the temporally correlated components of the measurement errors as well as any real, non-secular site motions as might arise from environmental loads [e.g., *Langbein*, 2008; *Bennett*, 2008]. Here, we assume that the informal factor of $\sim$2 inflation of uncertainties implied by the NRMS of 0.5 adequately approximates the true error statistics, noting that additional modest inflation of the velocity errors would not fundamentally change our conclusions.

[22] Our ability to resolve secular deformation within the plate boundary zone is independent of rigid-body translations and rotations of the entire network associated with the frame definition. Thus, this component of reference-frame error is of little consequence. However, common-mode periodic site motions may bias studies of strain rate, depending on the observation history at each station. *Blewitt and Lavallée* [2002] showed that, if unaccounted for, periodic-site motion would bias estimates for secular velocity depending on the duration of coordinate time series. If all stations of a local- or regional-scale network operated over precisely the same period of time, we would expect any velocity biases associated with these common-mode signals to also be common, and thus not contribute to estimates for strain rate, which are based on linear combinations of velocity differences. However, when coordinate time series data are measured for different time periods, biases may not cancel completely.

[23] The data set presented in this manuscript is quite heterogeneous, both in terms of observation strategy (campaign, semi-continuous, continuous) and observation period. For continuous stations, there is sufficient temporal density of data that periodic site motions can be estimated simultaneously with secular site motions. However, this is not the case for annual-campaign stations, and is only marginally true for semi-continuous stations. We attempted to mitigate the effect of periodic site motions on our campaign data set in three ways. First, our campaign observations were collected during the same season each year. Assuming that the amplitudes of the periodic motions are more or less constant, we expect the campaign monuments to sense the same repeating offsets each year. Second, we consider only stations that have been measured repeatedly over a period of >1.5 years. This helps to mitigate the biases associated with periodic motion, which decreases with time [*Blewitt and Lavallée*, 2002], even when the amplitudes of the periodic motions are not constant with time [*Bennett*, 2008]. Third, we reduced the campaign coordinate time series data set using the common mode periodic site motions obtained from the available continuous network of stations within our northern Italy study area. That is, we calculated the common-mode signal (CMS) motion for each epoch at each campaign station using the inferred CMS model derived from the CGPS data, and subtracted the calculated motion from each campaign time series.

5. Results

5.1. Time Series and Velocities

[24] Velocities obtained from the Common-mode Signal Reduced (CSR) time series are not expressed in the Eurasia frame because they have no net translational velocity. We derived "corrected" velocity estimates with respect to the Eurasia-fixed frame for all sites by adding the common-mode signal (CMS) velocity to the CSR velocity estimates for each station. We refer to the resulting estimates as Common-mode Seasonal Corrected (CSC) velocities.

[25] The horizontal components of the CSC velocity estimates, which are relative to the Eurasia reference frame, are plotted in Figure 6. Vertical velocity estimates determined from the CSR time series are shown in Figure 7. Because the common-mode vertical rate has been subtracted from the CSR time series these vertical rates refer to a no-net vertical frame of reference. The no-net-vertical frame determined here is similar in effect to some previous studies utilizing vertical rates for analysis of active tectonics [*Bennett and Hreinsdóttir*, 2007; *Bennett et al.*, 2007; *Hreinsdóttir and*

Table 1. Parameter Estimates for Common-Mode Signal Reduced Coordinate Time Series[a]

Site Information				North Component								East Component (mm/a)								Vertical Component (mm/a)							
Site Name[b]	Latitude	Longitude	Height (m)	V (mm/a)	σ (mm/a)	A (mm)	σ (mm)	SA (mm)	σ (mm)	NRMS	WRMS (mm)	V (mm/a)	σ (mm/a)	A (mm)	σ (mm)	SA (mm)	σ (mm)	NRMS	WRMS (mm)	V (mm/a)	σ (mm/a)	A (mm)	σ (mm)	SA (mm)	σ (mm)	NRMS	WRMS (mm)
ACOM(1)	46.5479	13.5149	1774.66	−0.264	0.018	0.184	0.075	0.14	0.074	0.511	1.009	0.102	0.015	0.296	0.063	0.088	0.062	0.749	1.242	1.511	0.066	1.505	0.271	0.62	0.267	0.643	4.599
AFAL(1)	46.5271	12.1745	2284.06	−0.467	0.023	0.409	0.093	0.016	0.09	0.487	1.113	−0.851	0.019	3.965	0.078	1.131	0.075	1.114	2.133	1.946	0.082	1.605	0.335	0.674	0.324	0.561	4.637
AGNE(1)	45.4679	7.13962	2354.59	−1.43	0.048	1.071	0.136	0.427	0.136	0.713	1.351	0.36	0.042	0.35	0.122	0.787	0.122	1.027	1.747	0.67	0.191	2.179	0.551	0.745	0.548	0.703	5.388
AJAC(1)	41.9275	8.76261	98.814	−0.675	0.011	0.51	0.048	0.359	0.047	0.768	1.157	−0.356	0.01	0.377	0.044	0.143	0.043	0.968	1.335	−0.289	0.044	1.549	0.187	0.573	0.183	0.778	4.574
ALES(1)	44.9231	8.61634	146.136	−0.265	0.091	1.636	0.167	0.377	0.144	0.451	1.143	−0.365	0.079	1.025	0.143	0.253	0.122	0.474	1.036	−0.795	0.344	0.878	0.63	0.112	0.538	0.507	4.869
ALPE(1)	45.0866	6.08346	1892.18	−0.927	0.053	0.563	0.119	0.187	0.114	0.583	1.106	0.043	0.044	0.288	0.1	0.207	0.096	0.807	1.294	0.602	0.196	3.007	0.446	1.865	0.426	0.608	4.323
AMPE(1)	46.4147	12.799	616.45	−0.029	0.046	0.266	0.119	0.248	0.118	0.491	1.214	0.025	0.039	0.402	0.1	0.202	0.099	0.462	0.965	1.361	0.169	1.61	0.44	0.517	0.435	0.543	4.982
ANCG(1)	43.6028	13.502	109.785	2.931	0.158	0.222	0.189	0.159	0.185	0.384	1.057	1.425	0.138	0.687	0.164	0.081	0.162	0.508	1.23	0.478	0.603	1.541	0.723	1.224	0.707	0.379	3.96
AQUI(1)	42.3682	13.3503	713.079	0.661	0.039	0.479	0.087	0.25	0.086	0.625	1.702	−0.859	0.034	0.746	0.076	0.146	0.075	0.794	1.913	0.635	0.146	1.87	0.331	1.057	0.325	0.599	6.216
AQUN(1)	42.3376	13.379	1012.65	0.612	0.266	1.318	0.265	0.493	0.245	0.55	1.528	−1.536	0.236	0.602	0.239	0.774	0.22	0.552	1.388	−1.439	1.021	2.144	1.032	0.934	0.951	0.456	4.947
APEZ(1)	43.4638	11.8749	328.294	0.57	0.127	0.586	0.151	0.262	0.146	0.465	1.087	1.098	0.113	0.183	0.133	0.137	0.129	0.575	1.246	0.153	0.482	1.61	0.576	0.917	0.554	0.497	4.163
ASIA(1)	45.8663	11.5254	1093.6	−0.128	0.059	0.153	0.123	0.327	0.119	0.508	1.645	−0.585	0.05	0.113	0.103	0.315	0.1	0.648	1.801	−0.89	0.22	0.724	0.452	0.556	0.439	0.546	5.576
ASTI(1)	44.9057	8.2032	207.048	−0.82	0.055	0.848	0.172	0.338	0.15	0.37	0.971	0.202	0.047	1.493	0.146	0.205	0.127	0.463	1.041	−0.27	0.204	0.472	0.642	1.021	0.556	0.461	4.522
BARC(1)	46.1931	12.5636	528.442	1.307	0.121	0.826	0.164	0.446	0.165	0.554	1.349	0.459	0.1	0.352	0.135	0.354	0.136	0.668	1.354	0.211	0.446	2.355	0.604	1.017	0.606	0.646	5.838
BASS(1)	45.7618	11.7314	168.65	0.371	0.169	0.526	0.215	0.463	0.204	0.341	0.993	0.697	0.145	0.978	0.184	0.335	0.176	0.474	1.192	−0.721	0.63	1.575	0.803	1.047	0.76	0.392	4.215
BIEL(1)	45.5608	8.04806	480.509	−1.152	0.059	0.264	0.156	0.262	0.151	0.408	1.271	0.137	0.05	0.528	0.13	0.235	0.127	0.522	1.377	−0.821	0.218	1.29	0.571	0.024	0.55	0.454	5.189
BORC(1)	44.3062	10.696	1023.39	−0.678	0.152	0.134	0.177	0.125	0.173	0.572	1.473	1.202	0.134	0.575	0.155	0.16	0.153	0.739	1.685	1.946	0.571	1.989	0.664	0.842	0.648	0.512	4.977
BORM(1)	46.4682	10.364	1263.35	−0.506	0.06	0.342	0.133	0.065	0.133	0.533	1.535	−1.023	0.049	0.913	0.11	0.077	0.11	0.61	1.466	0.825	0.219	2.97	0.487	0.96	0.484	0.528	5.59
BRAS(1)	44.1222	11.1131	901.141	0.424	0.009	0.296	0.053	0.177	0.052	1.047	1.779	0.065	0.008	0.166	0.046	0.212	0.045	0.891	1.335	0.393	0.034	2.104	0.203	0.591	0.199	0.833	5.406
BRBZ(1)	46.7966	11.9413	903.741	−0.506	0.067	0.732	0.119	0.273	0.115	0.48	1.286	0.068	0.055	0.225	0.098	0.306	0.096	0.473	1.054	2.421	0.239	2.218	0.428	0.537	0.416	0.498	4.817
BREA(1)	45.5649	10.2328	224.944	−0.445	0.028	3.446	0.088	0.703	0.084	0.571	1.164	−0.132	0.024	1.136	0.074	0.161	0.071	0.558	0.969	1.083	0.105	1.021	0.326	0.187	0.312	0.573	4.341
BRIX(1)	45.5649	10.2326	224.871	−0.553	0.021	2.447	0.105	0.43	0.099	0.441	1.001	−0.142	0.018	0.699	0.089	0.203	0.084	0.555	1.072	1.496	0.078	1.367	0.383	1.071	0.361	0.53	4.418
BRUG(1)	44.2364	9.72491	172.238	−0.101	0.248	0.858	0.21	0.77	0.2	0.473	1.53	0.639	0.215	0.307	0.185	0.387	0.176	0.483	1.389	−1.613	0.913	4.013	0.785	3.296	0.741	0.482	5.748
BZRG(1)	46.499	11.3368	329.121	−0.449	0.02	1.241	0.05	0.21	0.048	0.711	1.243	−0.97	0.017	0.474	0.042	0.016	0.04	0.929	1.362	1.117	0.074	1.571	0.187	0.436	0.178	0.812	5.321
CAIE(1)	43.4672	12.2479	352.116	0.737	0.133	0.243	0.207	0.223	0.183	0.463	1.043	0.383	0.114	0.535	0.175	0.194	0.156	0.557	1.076	−0.027	0.505	1.078	0.772	0.165	0.689	0.449	3.843
CALA(1)	43.8678	11.1643	117.966	0.429	0.095	0.617	0.146	0.265	0.141	0.545	1.26	1.279	0.084	0.782	0.128	0.162	0.125	0.627	1.284	0.738	0.363	2.942	0.553	0.902	0.535	0.556	4.883
CAME(1)	43.112	13.124	498.655	2.249	0.022	0.873	0.111	0.364	0.105	0.639	1.873	1.198	0.02	0.504	0.097	0.041	0.092	0.792	2.068	0.745	0.086	1.275	0.428	0.613	0.404	0.622	7.423
CANV(1)	46.0083	12.435	965.899	0.723	0.036	0.161	0.09	0.643	0.085	0.875	1.706	−0.541	0.031	0.206	0.078	0.312	0.073	0.849	1.441	0.379	0.136	0.351	0.347	0.525	0.325	0.545	4.156
CARP(1)	45.3682	10.4265	135.532	−0.706	0.091	0.396	0.156	0.134	0.153	0.403	0.894	0.074	0.079	0.447	0.134	0.235	0.133	0.463	0.891	0.355	0.338	2.414	0.576	0.913	0.565	0.461	3.781
CARZ(1)	46.0423	8.6802	1165.27	−0.911	0.047	0.381	0.124	0.281	0.121	0.738	1.316	−0.003	0.039	0.29	0.105	0.185	0.102	0.59	0.887	1.056	0.174	2.327	0.462	0.782	0.447	0.61	4.029
CASF(1)	43.4645	13.5439	227.221	2.068	2.688	0.383	1.141	0.231	0.364	0.348	0.904	3.004	2.388	1.266	1.006	0.282	0.321	0.438	1.003	9.294	10.121	3.421	4.293	1.366	1.378	0.426	4.218
CASX(1)	45.3867	7.7093	413.493	−1.177	0.089	0.477	0.178	0.172	0.174	0.452	1.073	−0.205	0.076	0.359	0.151	0.367	0.149	0.56	1.13	0.365	0.33	0.779	0.666	1.248	0.645	0.55	4.823
CAVA(1)	45.4794	12.5827	47.76	1.327	0.02	0.101	0.082	0.054	0.08	0.387	0.851	−0.185	0.017	0.221	0.069	0.201	0.066	0.435	0.802	−2.613	0.073	1.385	0.299	0.699	0.29	0.611	4.9
CHTL(1)	45.3041	6.35855	850.267	−1.102	0.011	0.313	0.07	0.136	0.067	0.723	1.407	−0.578	0.01	0.099	0.066	0.246	0.063	0.818	1.502	2.268	0.043	1.589	0.282	0.835	0.27	0.693	5.487
CITT(1)	43.4671	12.2479	351.467	0.783	0.222	0.646	0.22	0.155	0.213	0.411	1.091	0.251	0.196	0.922	0.193	0.189	0.189	0.508	1.19	−2.051	0.857	1.957	0.849	0.637	0.824	0.455	4.669
CNNS(1)	43.5546	7.01573	89.819	−1.159	0.039	0.453	0.112	0.193	0.107	0.389	0.912	0.418	0.033	0.332	0.097	0.103	0.092	0.511	1.04	−0.379	0.143	2.055	0.415	0.783	0.391	0.476	4.143
CODR(1)	45.9585	12.9791	91.882	0.753	0.093	0.814	0.161	0.414	0.158	0.285	0.796	0.147	0.078	0.589	0.135	0.206	0.133	0.368	0.889	1.345	0.344	0.882	0.596	0.243	0.583	0.364	3.745
COLD(1R)	43.3478	13.1218	506.452	1.844	0.055	1.156	0.134	0.323	0.135	0.797	2.3	0.766	0.047	0.223	0.115	0.183	0.117	1.258	3.152	−0.019	0.204	0.78	0.502	1.429	0.505	0.813	8.807
COMO(1)	45.8022	9.09562	292.267	−1.069	0.035	0.492	0.087	0.255	0.085	0.521	1.311	−0.193	0.03	2.087	0.074	0.22	0.071	0.525	1.124	0.638	0.13	2.11	0.32	0.394	0.309	0.516	4.784
CRE1(1)	45.1924	8.10576	211.18	−1.343	0.087	0.687	0.162	0.138	0.148	0.36	0.844	0.132	0.075	0.195	0.138	0.137	0.127	0.462	0.939	−0.404	0.324	2.799	0.603	1.406	0.549	0.508	4.429
CREA(1)	45.3543	9.68531	129.848	−0.571	0.042	0.394	0.101	0.07	0.1	0.348	0.761	−0.026	0.035	0.629	0.085	0.143	0.084	0.433	0.803	−1.276	0.152	1.193	0.367	0.681	0.361	0.485	3.872
CREX(1)	45.1467	10.002	102.674	0.051	0.031	0.317	0.095	0.021	0.093	0.431	0.926	0.119	0.026	0.179	0.08	0.09	0.079	0.453	0.83	−0.807	0.113	1.121	0.349	0.339	0.34	0.513	4.071
CSGP(1)	42.8549	13.5922	210.936	1.529	0.352	0.398	0.327	0.28	0.33	0.405	1.404	0.644	0.304	0.548	0.28	0.247	0.287	0.493	1.493	1.052	1.319	3.017	1.223	0.967	1.243	0.434	5.673
CUNE(1)	44.395	7.55357	598.11	−0.834	0.086	1.278	0.266	0.66	0.241	0.332	1.442	0.181	0.073	1.815	0.224	0.56	0.205	0.384	1.416	−1.643	0.319	2.735	0.988	0.342	0.889	0.501	7.963
DALM(1)	45.6463	9.59697	265.565	−0.74	0.039	0.341	0.108	0.324	0.105	0.411	0.927	0.038	0.033	0.935	0.091	0.192	0.089	0.459	0.876	0.522	0.145	0.865	0.4	0.201	0.388	0.48	4.001
DARF(1)	45.8803	10.1772	282.941	−0.355	0.175	0.733	0.211	0.107	0.199	0.488	1.396	0.371	0.153	0.687	0.183	0.29	0.174	0.673	1.687	0.385	0.664	2.739	0.8	1.093	0.755	0.454	4.955
DEVE(1)	46.3136	8.261	1679.41	−0.518	0.059	0.789	0.18	0.113	0.155	0.867	1.757	−0.19	0.057	0.085	0.173	0.109	0.15	1.032	2.025	0.769	0.256	1.858	0.775	1.874	0.666	0.788	6.887
ELBA(1)	42.7529	10.2111	271.733	−0.469	0.016	0.239	0.087	0.315	0.083	0.541	1.345	−0.72	0.014	0.16	0.078	0.012	0.074	0.698	1.555	0.073	0.061	0.651	0.336	0.857	0.321	0.616	5.934

Table 1. (continued)

Site Information				North Component								East Component (mm/a)								Vertical Component (mm/a)							
Site Name[b]	Latitude	Longitude	Height (m)	V (mm/a)	σ (mm/a)	A (mm)	σ (mm)	SA (mm)	σ (mm)	NRMS	WRMS (mm)	V (mm/a)	σ (mm/a)	A (mm)	σ (mm)	SA (mm)	σ (mm)	NRMS	WRMS (mm)	V (mm/a)	σ (mm/a)	A (mm)	σ (mm)	SA (mm)	σ (mm)	NRMS	WRMS (mm)
EMPO(1)	43.7151	10.9347	81.909	−1.087	0.103	1.816	0.164	0.46	0.152	0.402	1.008	0.076	0.09	0.391	0.144	0.175	0.134	0.454	1.012	−1.806	0.39	1.5	0.626	1.366	0.578	0.399	3.748
FAEZ(1)	44.3028	11.8613	83.838	2.245	0.128	0.661	0.15	0.401	0.146	0.447	1.016	0.957	0.111	0.236	0.13	0.399	0.128	0.527	1.046	−8.587	0.48	5.197	0.564	0.825	0.55	0.445	3.831
FERA(1)	44.8136	11.627	58.346	0.696	0.165	0.906	0.192	0.15	0.189	0.377	1.053	0.576	0.145	0.546	0.165	0.379	0.165	0.442	1.093	−0.866	0.616	2.34	0.721	0.874	0.711	0.442	4.558
FIGL(1)	43.6187	11.4735	188.039	0.879	0.12	0.727	0.182	0.167	0.173	0.452	1.25	−0.052	0.105	0.274	0.159	0.306	0.152	0.605	1.466	1	0.453	2.295	0.694	1.144	0.656	0.472	4.973
FIRE(1)	44.1183	11.378	487.584	1.126	0.103	0.559	0.155	0.293	0.15	1.021	2.513	−0.101	0.09	1.871	0.135	0.356	0.131	0.778	1.677	−0.081	0.388	1.023	0.584	1.33	0.564	0.565	5.29
FOLI(1)	42.9549	12.6988	296.333	0.616	0.209	0.205	0.182	0.169	0.167	0.458	1.158	−1.1	0.184	0.567	0.161	0.547	0.148	0.666	1.506	0.428	0.789	1.097	0.695	0.707	0.635	0.525	5.071
FOSS(1)	43.689	12.8066	176.507	1.906	0.162	0.403	0.189	0.141	0.187	0.733	2.068	1.771	0.142	0.309	0.165	0.577	0.164	0.672	1.676	−0.407	0.618	1.744	0.723	0.693	0.714	0.5	5.407
FUSE(1)	46.4142	13.0012	581.918	−0.023	0.074	0.433	0.129	0.147	0.127	0.563	1.203	0.152	0.064	0.473	0.111	0.08	0.109	0.525	0.973	−0.545	0.277	1.532	0.486	0.224	0.474	0.53	4.28
GAVI(1)	45.8493	8.70263	343.689	−1.246	0.03	2.629	0.093	0.59	0.088	0.861	1.786	0.399	0.025	1.627	0.078	0.124	0.074	0.824	1.453	−0.332	0.11	0.942	0.343	0.299	0.325	0.6	4.605
GENO(1)	44.4194	8.92114	155.539	−1.005	0.011	0.391	0.082	0.211	0.08	0.441	1.194	−0.018	0.01	0.458	0.071	0.053	0.069	0.492	1.152	−0.477	0.043	0.557	0.316	0.18	0.306	0.509	5.275
GENV(1)	44.4152	8.88087	61.558	−0.94	0.193	0.768	0.226	0.201	0.222	0.367	1.193	0.101	0.168	0.324	0.196	0.2	0.194	0.401	1.133	0.781	0.75	2.609	0.878	1.203	0.859	0.353	4.468
GORI(1)	45.9433	13.6238	153.42	0.64	0.166	0.347	0.216	0.301	0.219	0.34	1.095	−0.042	0.14	0.78	0.181	0.282	0.185	0.335	0.915	−0.84	0.594	2.365	0.773	0.491	0.783	0.398	4.609
GRAM(1)	42.9755	13.8705	64.407	2.876	0.278	1.087	0.183	0.203	0.175	0.404	0.987	3.179	0.247	0.411	0.162	0.087	0.157	0.521	1.152	−2.061	1.068	1.868	0.704	0.989	0.687	0.432	4.229
GRAS(1)	43.7547	6.92057	1319.31	−0.96	0.012	0.563	0.045	0.33	0.043	0.777	1.216	−0.117	0.011	0.496	0.04	0.278	0.039	0.925	1.313	−0.618	0.049	0.414	0.174	0.863	0.168	0.731	4.516
GRAV(1)	45.1277	7.01659	840.153	−1.494	0.109	0.447	0.195	0.482	0.177	0.831	2.193	0.765	0.091	0.275	0.163	0.574	0.148	0.957	2.122	−0.022	0.401	5.708	0.726	2.528	0.651	0.704	6.862
GROG(1)	43.4263	9.892	241.057	−0.687	0.06	0.436	0.112	0.188	0.11	0.358	0.737	−0.007	0.052	0.533	0.095	0.249	0.095	0.479	0.847	0.097	0.228	2.049	0.422	0.716	0.416	0.435	3.391
GUIE(1)	43.3518	12.5654	530.456	2.166	0.247	0.709	0.241	0.56	0.23	0.524	1.299	1.468	0.211	0.558	0.207	0.231	0.199	0.598	1.287	−1.506	0.937	0.833	0.919	1.84	0.878	0.462	4.399
IEMO(1)	43.5917	12.0532	450.681	1.428	0.134	4.04	0.186	0.245	0.202	0.709	1.569	−0.323	0.115	0.121	0.157	0.164	0.173	0.78	1.498	4.46	0.508	0.667	0.696	0.674	0.764	0.6	5.054
IENG(1)	45.0151	7.63941	316.599	−1.302	0.023	0.581	0.092	0.433	0.089	0.529	1.207	0.405	0.02	0.851	0.078	0.482	0.075	0.535	1.052	0.562	0.085	1.619	0.337	0.488	0.323	0.518	4.342
IGMI(1)	43.7957	11.2138	95.065	1.394	0.123	1.926	0.135	0.122	0.126	0.423	1.017	0.122	0.106	0.129	0.116	0.267	0.109	0.433	0.9	−1.11	0.472	0.747	0.521	1.107	0.485	0.494	4.584
INGP(1)	42.3825	13.3156	731.828	1.78	0.068	0.597	0.088	0.161	0.085	0.824	1.649	0.389	0.059	0.736	0.077	0.111	0.075	1.09	1.926	0.675	0.261	1.351	0.34	1.277	0.331	0.839	6.523
INGR(1)	41.8281	12.5148	104.486	0.74	0.022	0.545	0.07	0.239	0.068	0.502	1.11	−1.058	0.019	2.698	0.061	0.464	0.06	0.648	1.269	0.54	0.086	0.635	0.269	0.778	0.261	0.534	4.574
ITFA(1)	43.3437	12.9262	401.724	2.005	0.058	0.491	0.125	0.059	0.115	0.608	1.378	0.715	0.051	1.386	0.108	0.293	0.1	0.995	1.963	0.105	0.223	0.278	0.473	0.242	0.438	0.676	5.855
ITGT(1)	43.2337	12.7821	572.281	1.919	0.05	1.599	0.116	0.284	0.109	0.747	1.667	1.505	0.043	1.287	0.1	0.233	0.095	1.399	2.721	−0.07	0.188	0.573	0.442	0.538	0.416	0.928	7.932
ITRA(1)	42.6585	14.0018	105.786	1.868	0.058	0.855	0.134	0.291	0.131	0.457	1.082	1.147	0.051	0.208	0.117	0.17	0.116	0.481	1.004	0.564	0.222	1.201	0.513	0.548	0.505	0.476	4.361
ITRN(1)	44.0483	12.5821	57.729	0.977	0.285	0.865	0.475	0.477	0.332	0.327	0.685	0.586	0.238	2.058	0.414	0.54	0.289	0.459	0.829	1.175	1.07	2.187	1.765	1.887	1.257	0.416	3.3
JANU(1)	44.9104	6.71003	2583.85	−0.929	0.101	0.391	0.221	0.429	0.222	0.679	1.283	0.193	0.087	0.281	0.184	0.189	0.19	0.662	1.064	−0.166	0.375	4.87	0.808	1.462	0.818	0.816	5.676
JOAN(1)	46.184	13.4161	1190.47	0.707	0.066	0.13	0.115	0.128	0.114	0.431	0.891	−0.218	0.055	0.402	0.096	0.359	0.096	0.549	0.957	−1.074	0.241	0.773	0.42	0.057	0.415	0.52	3.928
KOE2(1)	46.6742	13.0094	755.983	−0.118	0.171	1.158	0.242	0.406	0.241	0.583	1.862	0.273	0.144	3.02	0.2	0.2	0.2	0.49	1.309	1.492	0.628	1.305	0.885	1.006	0.878	0.563	6.593
KOET(1)	46.6742	13.0094	755.99	−0.755	0.066	0.466	0.126	0.458	0.123	0.716	2.066	−0.462	0.053	2.431	0.103	0.142	0.101	0.655	1.567	3.372	0.235	2.645	0.455	0.652	0.445	0.591	6.211
LANK(1)	46.6308	13.8928	583.054	0.348	0.081	0.12	0.2	0.718	0.194	0.605	2.074	0.658	0.067	0.784	0.164	0.36	0.161	0.604	1.725	−1.256	0.288	2.896	0.709	1.868	0.689	0.584	7.095
LASP(1)	44.0733	9.83965	87.128	−0.692	0.03	0.081	0.091	0.169	0.088	0.504	1.074	0.256	0.026	0.178	0.078	0.115	0.076	0.573	1.056	−0.138	0.114	1.004	0.34	1.045	0.33	0.542	4.353
LAT1(1)	41.4708	12.9015	97.844	0.423	0.234	0.633	0.208	0.154	0.203	0.368	1.046	−1.634	0.209	2.129	0.188	0.398	0.183	0.486	1.255	4.676	0.905	1.732	0.81	1.286	0.791	0.401	4.34
LEC1(1)	45.8573	9.40696	310.859	−0.77	0.024	0.689	0.113	0.385	0.103	0.51	1.217	−0.433	0.02	0.257	0.095	0.393	0.087	0.586	1.185	1.192	0.088	0.69	0.422	0.412	0.385	0.556	5.173
LECC(1)	45.8573	9.40692	311.061	−1.168	0.031	0.565	0.097	0.286	0.091	0.469	1.104	−0.572	0.027	0.608	0.082	0.316	0.077	0.549	1.117	0.588	0.119	0.845	0.367	0.139	0.344	0.55	5.041
LODI(1)	45.2869	9.47258	126.427	−0.572	0.142	0.756	0.218	0.091	0.216	0.526	1.874	0.352	0.12	1.473	0.189	0.07	0.187	0.496	1.64	−0.197	0.533	2.093	0.832	0.685	0.819	0.499	6.345
LUCX(1)	43.85	10.4997	69.994	0.161	0.117	0.845	0.173	0.361	0.169	0.466	1.289	0.57	0.104	0.143	0.156	0.295	0.153	0.523	1.317	−0.444	0.436	2.316	0.653	2.85	0.635	0.449	4.596
MABZ(1)	46.686	10.551	1092.03	−0.259	0.063	0.221	0.106	0.088	0.104	0.505	1.215	0.052	0.052	0.539	0.087	0.264	0.086	0.667	1.33	1.859	0.232	1.89	0.389	0.995	0.383	0.574	5.089
MACE(1)	43.2941	13.4509	307.097	2.77	0.29	0.111	0.186	0.279	0.175	0.437	1.123	1.263	0.256	0.414	0.163	0.278	0.155	0.513	1.171	−1.857	1.091	1.871	0.7	0.174	0.655	0.48	4.656
MANT(1)	45.1601	10.7894	78.566	−0.04	0.036	1.036	0.099	0.147	0.096	0.467	0.938	0.016	0.031	0.598	0.083	0.117	0.082	0.48	0.825	−0.142	0.135	0.914	0.365	0.344	0.355	0.514	3.826
MAON(1)	42.4282	11.1307	228.375	−0.578	0.025	0.026	0.073	0.115	0.07	0.779	1.367	−0.786	0.022	0.215	0.063	0.1	0.062	0.606	0.938	0.077	0.095	1.046	0.278	0.405	0.269	0.662	4.461
MDEA(1)	45.9245	13.4356	165.684	1.386	0.021	0.232	0.091	0.087	0.086	0.366	0.835	−0.46	0.018	0.164	0.076	0.142	0.072	0.482	0.939	0.376	0.078	0.498	0.338	0.513	0.321	0.505	4.396
MEDI(1)	44.52	11.6468	50.05	1.077	0.006	1.038	0.033	0.241	0.031	1.263	1.627	1.421	0.006	1.386	0.029	0.324	0.029	1.273	1.469	−1.651	0.026	0.488	0.13	0.538	0.125	0.965	4.917
MILA(1)	45.48	9.22935	187.244	−0.298	0.031	0.751	0.093	0.142	0.09	0.438	0.912	−0.174	0.026	0.446	0.078	0.101	0.076	0.522	0.925	−0.813	0.115	1.513	0.342	0.424	0.333	0.52	4.022
MODA(1)	45.2138	6.71008	1182.22	−1.175	0.011	0.699	0.076	0.105	0.075	0.935	2.137	−0.295	0.009	0.115	0.062	0.17	0.062	0.843	1.576	1.793	0.04	0.966	0.274	0.648	0.27	0.718	5.941
MODP(1)	44.629	10.9487	92.169	2.566	0.044	1.271	0.111	0.09	0.108	0.381	0.847	0.245	0.038	1.059	0.094	0.376	0.092	0.45	0.863	−6.966	0.168	2.73	0.416	0.584	0.404	0.625	5.244
MOGG(1)	46.4067	13.1983	377.95	0.322	0.038	0.404	0.103	0.05	0.1	0.723	1.585	−0.216	0.032	0.232	0.086	0.169	0.084	0.667	1.244	0.715	0.144	3.46	0.387	0.103	0.375	0.647	5.385
MOIE(1)	43.5032	13.1235	174.916	2.147	0.079	0.097	0.21	0.06	0.209	0.405	1.414	1.29	0.069	0.274	0.181	0.267	0.181	0.419	1.274	1.739	0.303	0.814	0.794	1.132	0.791	0.406	5.404

Table 1. (continued)

Site Information				North Component								East Component (mm/a)								Vertical Component (mm/a)							
Site Name[b]	Latitude	Longitude	Height (m)	V (mm/a)	σ (mm/a)	A (mm)	σ (mm)	SA (mm)	σ (mm)	NRMS	WRMS (mm)	V (mm/a)	σ (mm/a)	A (mm)	σ (mm)	SA (mm)	σ (mm)	NRMS	WRMS (mm)	V (mm/a)	σ (mm/a)	A (mm)	σ (mm)	SA (mm)	σ (mm)	NRMS	WRMS (mm)
MONC(1)	45.0739	7.92722	464.459	−1.173	0.044	0.828	0.109	0.097	0.106	0.404	0.898	0.322	0.037	0.189	0.091	0.072	0.089	0.441	0.825	−1.713	0.168	2.229	0.413	0.088	0.399	0.516	4.37
MOND(1)	44.3889	7.8272	580.585	−1.205	0.043	0.703	0.134	0.268	0.123	0.377	0.901	0.354	0.038	0.482	0.116	0.223	0.106	0.464	0.973	0.632	0.168	0.444	0.527	0.564	0.478	0.612	5.744
MOPS(1)	44.6294	10.9492	92.203	2.05	0.068	0.439	0.131	0.089	0.126	0.409	0.966	0.637	0.058	0.946	0.111	0.267	0.108	0.618	1.258	−4.042	0.252	1.93	0.487	0.946	0.468	0.554	4.899
MORO(1)	42.0525	12.6191	201.581	1.489	0.332	0.81	0.23	0.531	0.213	0.367	1.088	−3.349	0.299	1.708	0.205	0.22	0.192	0.43	1.124	−0.806	1.281	1.627	0.881	1.602	0.817	0.428	4.758
MOZZ(1)	43.9788	10.5443	156.338	−0.561	0.341	0.388	0.3	0.21	0.285	0.374	1.262	−0.142	0.303	0.796	0.269	0.551	0.256	0.507	1.532	1.104	1.304	3.585	1.173	1.021	1.101	0.564	7.383
MPRA(1)	46.2408	12.9877	808.549	0.27	0.019	0.781	0.091	0.452	0.088	0.584	1.447	−0.676	0.016	0.582	0.076	0.431	0.074	0.518	1.086	0.252	0.069	0.148	0.33	0.541	0.319	0.497	4.499
MRGE(1)	45.7698	7.06108	1722.77	−1.586	0.05	0.631	0.115	0.45	0.11	0.626	1.301	−0.037	0.042	0.665	0.095	0.142	0.092	0.718	1.242	0.914	0.184	1.476	0.423	1.855	0.405	0.666	5.113
MSEL(1)	44.52	11.6465	49.346	1.434	0.037	0.741	0.13	0.059	0.127	0.412	1.239	0.966	0.032	0.049	0.111	0.017	0.109	0.351	0.91	−2.302	0.141	1.042	0.494	0.684	0.482	0.392	4.474
MSTR(1)	45.4904	12.2386	68.127	−0.567	0.182	2.235	0.195	0.312	0.197	0.368	0.989	−0.078	0.157	0.571	0.167	0.21	0.17	0.419	1.008	−1.091	0.682	4.822	0.733	1.129	0.738	0.383	3.8
NICA(1)	43.7033	7.22726	256.475	−1.016	0.037	0.446	0.116	0.033	0.116	0.398	0.99	0.178	0.032	0.307	0.099	0.209	0.1	0.413	0.902	−0.502	0.139	1.019	0.428	0.796	0.426	0.433	3.988
NICE(1)	43.7255	7.29998	427.302	−0.864	0.014	0.35	0.08	0.19	0.077	0.535	1.244	0.055	0.012	0.268	0.069	0.085	0.066	0.474	0.959	0.323	0.052	0.801	0.296	0.808	0.284	0.483	4.196
NOVA(1)	45.4472	8.61397	218.561	−0.776	0.017	1.243	0.107	0.087	0.103	0.478	1.308	−0.266	0.015	0.24	0.094	0.139	0.091	0.492	1.192	0.63	0.062	0.619	0.396	0.756	0.381	0.474	4.8
NOVG(1)	45.8964	13.6247	110.158	0.989	0.131	0.692	0.142	0.056	0.132	0.52	1.226	−0.394	0.11	0.716	0.118	0.24	0.111	0.478	0.947	0.347	0.483	2.132	0.523	0.55	0.487	0.532	4.593
OATO(1)	45.0416	7.7653	658.807	−2.108	0.053	0.523	0.159	0.198	0.153	0.371	0.972	0.209	0.045	0.637	0.135	0.314	0.13	0.45	0.997	−0.676	0.201	2.4	0.61	1.327	0.584	0.457	4.541
OLGI(1)	42.0547	12.3552	207.868	0.033	0.28	0.658	0.211	0.231	0.188	0.38	0.933	−2.629	0.253	0.233	0.188	0.189	0.169	0.462	1.026	−3.192	1.076	3.429	0.811	0.801	0.719	0.45	4.247
PADO(1)	45.4112	11.8961	64.689	0.38	0.017	2.549	0.08	0.297	0.079	0.629	1.479	0.166	0.015	1.307	0.068	0.229	0.067	0.597	1.203	0.437	0.063	0.539	0.297	0.183	0.292	0.516	4.517
PALN(1)	45.9047	13.3076	85.201	0.87	0.041	0.114	0.107	0.035	0.105	0.384	0.865	−0.539	0.034	0.643	0.09	0.147	0.089	0.377	0.726	0.747	0.149	0.256	0.391	0.249	0.385	0.464	3.854
PALX(1)	45.6021	9.89731	238.741	−1.49	0.088	0.532	0.191	0.12	0.173	0.51	1.36	−0.866	0.074	2.278	0.164	0.468	0.151	0.595	1.401	3.334	0.32	3.212	0.704	1.149	0.639	0.589	5.738
PARM(1)	44.7646	10.3122	121.818	0.755	0.029	1.863	0.085	0.321	0.079	0.505	0.921	0.739	0.025	0.507	0.072	0.215	0.068	0.581	0.909	0.064	0.109	5.55	0.317	1.23	0.297	0.614	4.209
PARO(1)	44.446	8.08113	849.754	−1.233	0.105	0.525	0.146	0.208	0.149	0.449	0.903	0.638	0.092	0.31	0.126	0.075	0.128	0.497	0.858	−0.811	0.398	1.582	0.555	0.698	0.562	0.443	3.379
PAVI(1)	45.203	9.13614	143.644	−0.441	0.034	0.877	0.085	0.064	0.082	0.375	0.889	−0.153	0.029	1.832	0.072	0.287	0.07	0.642	1.307	−0.849	0.127	1.314	0.311	0.845	0.3	0.543	4.756
PAZO(1)	45.8057	13.0526	50.086	0.701	0.105	0.177	0.167	0.133	0.162	0.304	0.769	−0.186	0.09	0.445	0.142	0.304	0.138	0.371	0.815	0.717	0.388	0.914	0.616	1.012	0.593	0.404	3.737
PENB(1)	43.8173	12.2651	617.001	3.198	0.263	0.064	0.181	0.157	0.182	0.63	1.625	2.704	0.293	0.849	0.166	0.23	0.176	0.604	1.41	−0.83	0.99	1.637	0.684	1.183	0.69	0.537	5.279
PERU(1)	43.111	12.3936	471.593	0.899	0.119	0.264	0.164	0.202	0.164	0.48	1.168	−0.209	0.103	0.116	0.142	0.097	0.143	0.515	1.102	1.442	0.449	1.132	0.62	0.723	0.622	0.549	5.108
PIAX(1)	45.0432	9.68979	115.302	0.014	0.146	1.765	0.177	0.65	0.174	0.489	1.267	0.255	0.127	1.218	0.153	0.206	0.151	0.45	1.017	1.231	0.542	0.665	0.658	0.908	0.645	0.509	4.931
PILA(1)	46.5656	11.9062	2141.71	0.358	0.166	1.212	0.277	0.847	0.275	0.464	2.04	0.864	0.138	0.736	0.229	0.732	0.23	0.433	1.615	3.036	0.582	2.274	0.975	1.169	0.964	0.287	4.375
PISA(1)	43.7475	10.3661	56.871	−0.426	0.101	0.497	0.154	0.375	0.148	0.385	0.954	0.141	0.089	0.884	0.137	0.142	0.132	0.453	1.007	−0.89	0.383	4.341	0.586	1.551	0.56	0.562	5.192
PORA(1)	45.886	10.1088	1927.31	−1.589	0.053	0.923	0.107	0.81	0.108	0.771	1.345	1.062	0.044	1.017	0.089	0.624	0.091	0.982	1.451	−1.883	0.195	0.221	0.395	0.377	0.397	0.699	4.492
PORD(1)	45.9568	12.6612	81.75	0.319	0.039	0.823	0.103	0.146	0.101	0.461	1.013	−0.391	0.033	0.569	0.087	0.133	0.086	0.417	0.783	1.09	0.144	0.116	0.38	0.504	0.374	0.492	4.014
POZZ(1)	46.4226	11.6817	1392.5	−0.449	0.215	0.221	0.21	0.266	0.195	0.569	1.809	0.967	0.182	1.366	0.177	0.216	0.166	0.706	1.698	0.247	0.806	1.321	0.783	1.956	0.727	0.604	5.646
PQRL(1)	42.9833	6.20609	112.272	−1.375	0.067	1.284	0.119	0.41	0.117	0.552	1.481	0.731	0.061	0.334	0.106	0.12	0.105	0.654	1.595	−0.663	0.25	2.119	0.465	0.368	0.45	1.46	13.7
PRAT(1)	43.8856	11.0991	119.969	0.96	0.011	0.467	0.081	0.187	0.078	0.555	1.463	0.292	0.009	0.515	0.068	0.027	0.066	0.56	1.245	−0.576	0.041	0.658	0.308	0.225	0.298	0.557	5.607
PSTE(1)	42.428	11.1202	72.368	−0.814	0.151	1.291	0.184	0.145	0.179	0.679	1.774	−0.392	0.137	0.541	0.166	0.23	0.162	0.607	1.441	−1.575	0.592	2.52	0.724	1.559	0.7	0.501	5.162
PTOL(1)	44.9515	12.3341	49.329	0.629	0.237	0.733	0.231	0.06	0.228	0.407	1.569	1.119	0.206	0.859	0.199	0.451	0.199	0.455	1.495	−5.179	0.879	1.399	0.838	0.808	0.827	0.419	5.45
PUGS(1)	44.8769	13.8487	68.271	1.674	0.269	0.75	0.497	0.857	0.375	0.396	1.02	0.705	0.235	0.596	0.411	0.724	0.315	0.531	1.149	−0.772	1.001	2.169	1.787	2.151	1.361	0.402	3.774
PUYA(1)	44.8577	6.47895	1690.24	−1.452	0.035	0.687	0.097	0.217	0.091	0.712	1.28	0.724	0.031	1.247	0.085	0.296	0.08	1.086	1.713	1.319	0.136	1.885	0.372	1.297	0.35	0.741	5.113
PVIA(1)	45.2028	9.13666	150.079	−0.624	0.027	1.844	0.083	0.13	0.081	0.592	1.13	0.199	0.023	0.865	0.07	0.068	0.068	0.656	1.064	−0.693	0.1	1.326	0.309	0.54	0.298	0.578	4.102
RABU(1)	44.2678	6.97706	2551.76	−1.16	0.022	2.323	0.088	0.717	0.084	0.664	1.838	0.371	0.019	2.851	0.075	1.465	0.072	0.878	2.22	0.654	0.08	1.239	0.316	0.995	0.302	0.759	6.184
RADO(1)	46.3438	14.1716	554.355	0.435	0.055	1.147	0.139	0.217	0.135	0.609	1.535	0.452	0.046	1.417	0.115	0.203	0.113	0.695	1.476	0.579	0.203	0.321	0.508	0.469	0.491	0.644	5.922
REFO(1)	42.9557	12.7035	306.602	0.817	0.083	1.126	0.144	0.029	0.142	0.591	1.647	0.288	0.072	1.188	0.125	0.189	0.123	0.935	2.311	−0.283	0.318	1.035	0.552	0.592	0.543	0.504	5.354
REMO(1)	43.4525	12.2256	476.558	2.489	0.063	1.208	0.124	0.406	0.11	0.618	1.284	1.936	0.055	0.63	0.107	0.432	0.095	0.822	1.482	−1.227	0.235	0.922	0.464	0.766	0.409	0.543	4.244
RENO(1)	42.7928	13.0931	669.08	0.933	0.054	0.185	0.115	0.104	0.105	0.618	1.374	0.872	0.047	0.272	0.1	0.299	0.092	0.7	1.5	−1.657	0.203	1.492	0.433	0.208	0.398	0.719	5.975
REPI(1)	42.9521	12.0024	575.717	0.915	0.045	0.639	0.091	0.147	0.088	0.524	1.01	−0.365	0.04	0.412	0.079	0.184	0.076	0.668	1.126	1.354	0.172	1.29	0.343	0.319	0.331	0.6	4.394
RETO(1)	42.7823	12.4069	466.336	0.52	0.064	0.26	0.137	0.201	0.134	0.432	1.186	−0.379	0.056	0.212	0.118	0.1	0.117	0.476	1.146	1.907	0.241	2.068	0.512	0.152	0.499	0.487	5.036
RIET(1)	42.4076	12.8572	457.191	−1.716	0.196	1.173	0.179	0.214	0.168	0.569	1.407	0.246	0.178	0.718	0.163	0.191	0.154	0.609	1.392	−3.226	0.709	2.101	0.651	1.412	0.611	0.58	5.288
ROMA(1)	41.9049	12.422	146.043	−0.007	0.315	0.832	0.21	0.148	0.193	0.293	0.785	−2.472	0.283	0.461	0.187	0.18	0.173	0.353	0.85	−3.06	1.212	1.36	0.804	0.711	0.737	0.38	3.914
RONC(1)	45.9841	10.6698	885.435	0.973	0.221	0.846	0.225	0.099	0.206	0.668	1.687	−0.508	0.194	1.06	0.198	0.837	0.181	0.767	1.681	−1.058	0.851	2.824	0.862	2.025	0.785	0.6	5.605
ROSD(1)	45.6915	6.62823	1694.47	−1.216	0.047	0.855	0.113	0.68	0.107	0.647	1.346	−0.431	0.041	2.259	0.094	1.103	0.089	0.985	1.741	1.11	0.18	1.094	0.421	1.26	0.397	0.708	5.598

Table 1. (continued)

Site Information				North Component								East Component (mm/a)								Vertical Component (mm/a)							
Site Name[b]	Latitude	Longitude	Height (m)	V (mm/a)	σ (mm/a)	A (mm)	σ (mm)	SA (mm)	σ (mm)	NRMS	WRMS (mm)	V (mm/a)	σ (mm/a)	A (mm)	σ (mm)	SA (mm)	σ (mm)	NRMS	WRMS (mm)	V (mm/a)	σ (mm/a)	A (mm)	σ (mm)	SA (mm)	σ (mm)	NRMS	WRMS (mm)
ROVE(1)	45.8935	11.0421	261.656	0.018	0.071	1.268	0.124	0.12	0.119	0.38	1.21	−0.168	0.059	0.662	0.103	0.289	0.099	0.486	1.311	0.178	0.262	1.996	0.456	0.981	0.437	0.46	5.427
ROVI(1)	45.0866	11.7828	62.781	0.713	0.042	0.356	0.135	0.12	0.133	0.432	1.483	−0.404	0.036	0.963	0.114	0.139	0.113	0.53	1.565	−0.816	0.158	1.329	0.499	0.515	0.494	0.481	5.091
RSMN(1)	43.9335	12.4507	767.463	2.11	0.036	0.296	0.107	0.156	0.106	0.555	1.302	1.041	0.032	1.162	0.092	0.2	0.091	0.718	1.464	1.815	0.138	1.683	0.401	0.894	0.397	0.705	6.259
RSTO(1)	42.6584	14.0015	102.575	1.781	0.018	0.857	0.081	0.05	0.077	0.604	1.335	0.791	0.016	0.254	0.071	0.057	0.068	0.653	1.278	0.262	0.069	0.752	0.31	0.323	0.296	0.526	4.476
SARN(1)	46.4187	11.1416	1049.69	0.016	0.209	0.374	0.21	0.268	0.193	0.402	0.928	1.135	0.178	0.567	0.177	0.106	0.163	0.52	0.988	0.012	0.771	0.538	0.772	0.992	0.706	0.532	4.263
SAVX(1)	44.6476	7.66067	380.445	−1.214	0.042	0.257	0.132	0.316	0.125	0.534	1.161	0.45	0.036	0.232	0.113	0.316	0.107	0.591	1.107	−0.203	0.157	2.08	0.496	0.438	0.467	0.507	4.126
SBPO(1)	45.051	10.9198	62.419	0.212	0.027	0.425	0.082	0.249	0.08	0.426	0.786	−0.321	0.023	0.352	0.069	0.239	0.068	0.474	0.748	−0.441	0.102	0.95	0.305	0.8	0.296	0.515	3.55
SCHI(1)	45.7181	11.363	254.683	0.225	0.168	0.152	0.202	0.262	0.2	0.459	1.379	−0.04	0.144	0.603	0.171	0.08	0.171	0.524	1.354	0.211	0.612	2.294	0.735	1.393	0.725	0.643	7.062
SGIP(1)	44.6355	11.1827	63.486	0.517	0.043	0.43	0.105	0.188	0.101	0.587	1.217	1.536	0.036	0.34	0.089	0.352	0.087	0.696	1.246	−6.102	0.16	1.758	0.394	0.492	0.379	0.498	3.872
SOPH(1)	43.6114	7.0541	178.814	−1.064	0.013	0.725	0.075	0.131	0.073	0.426	0.957	−0.008	0.012	0.451	0.066	0.097	0.063	0.489	0.959	0.09	0.05	0.671	0.283	0.637	0.272	0.485	4.101
SPEL(1R)	42.9972	12.6716	352.261	1.782	0.067	0.516	0.142	0.21	0.142	0.505	1.364	0.547	0.059	0.396	0.122	0.388	0.123	0.718	1.691	−3.112	0.254	0.988	0.537	0.142	0.535	0.525	5.393
SPER(1)	46.0694	11.5094	604.826	0.013	0.218	0.822	0.209	0.43	0.192	0.557	1.69	0.619	0.185	0.608	0.176	0.25	0.162	0.601	1.461	−0.182	0.807	1.961	0.771	1.01	0.704	0.566	5.362
STBZ(1)	46.8983	11.4256	1043.71	−0.302	0.061	0.206	0.104	0.152	0.101	0.543	1.288	0.39	0.051	0.845	0.088	0.266	0.086	0.607	1.23	2.178	0.23	1.57	0.392	0.467	0.383	0.543	4.897
TARV(1)	46.5024	13.5926	761.133	−0.113	0.078	2.985	0.105	0.32	0.106	0.833	1.409	0.39	0.066	0.123	0.088	0.039	0.09	0.916	1.318	1.289	0.286	2.286	0.385	0.342	0.39	1.01	6.293
TEOL(1)	45.3428	11.6773	203.39	0.847	0.023	0.292	0.086	0.032	0.083	0.399	0.823	−0.47	0.019	0.204	0.073	0.1	0.071	0.527	0.925	−0.483	0.085	0.511	0.32	0.474	0.309	0.507	3.884
TERA(1)	42.6571	13.6981	310.361	0.973	0.577	0.845	0.304	0.737	0.256	0.565	1.723	2.098	0.523	1.042	0.275	0.73	0.234	0.62	1.734	−3.966	2.291	4.408	1.201	2.318	1.013	0.447	5.454
TGPO(1)	45.0031	12.2283	49.39	0.182	0.123	2.758	0.241	0.627	0.232	0.325	1.011	0.3	0.105	1.168	0.203	0.247	0.197	0.343	0.888	−5.888	0.451	1.305	0.877	2.246	0.844	0.448	4.982
TODI(1)	42.7808	12.4079	444.117	1.145	0.623	0.73	0.692	0.668	0.684	0.777	7.779	0.226	0.565	1.509	0.635	1.155	0.624	0.973	9.365	−0.021	3.421	5.875	3.707	5.451	3.732	0.501	12.786
TOLF(1)	42.064	12	362.765	0.557	0.046	1.47	0.107	0.401	0.098	0.491	1.06	−1.505	0.041	3.036	0.093	0.645	0.086	0.893	1.717	−0.099	0.179	3.993	0.409	0.918	0.376	0.444	3.697
TORI(1)	45.0634	7.66128	310.739	−0.894	0.012	1.259	0.076	0.22	0.073	0.467	1.251	−0.093	0.011	1.449	0.065	0.168	0.063	0.521	1.199	0.243	0.047	1.497	0.287	0.191	0.277	0.543	5.504
TREP(1)	45.4677	12.4547	51.332	0.688	0.105	0.28	0.252	0.361	0.209	0.262	0.778	1.265	0.087	0.434	0.209	0.436	0.174	0.343	0.85	−10.659	0.386	1.539	0.919	0.601	0.77	0.428	4.693
TREX(1)	46.0909	11.1183	275.3	−0.616	0.204	1.279	0.197	0.226	0.182	0.542	1.508	1.703	0.176	1.364	0.166	0.829	0.154	0.764	1.726	0.167	0.778	2.739	0.744	1.536	0.685	0.613	5.802
TRI2(1)	45.6606	13.7878	161.588	1.286	0.043	0.452	0.111	0.148	0.11	0.402	0.942	−0.251	0.037	1.208	0.094	0.152	0.094	0.557	1.124	0.392	0.16	1.56	0.414	0.582	0.41	0.518	4.559
TRIE(1)	45.7098	13.7635	323.395	1.315	0.017	0.138	0.075	0.161	0.073	0.475	0.975	−0.623	0.014	1.181	0.064	0.393	0.061	0.682	1.192	0.481	0.061	0.808	0.275	0.576	0.265	0.551	4.147
TROP(1)	43.2195	6.60101	369.309	−1.106	0.043	0.36	0.125	0.085	0.114	0.513	1.101	−0.036	0.037	0.264	0.107	0.04	0.099	0.586	1.091	−0.416	0.162	2.105	0.472	0.054	0.431	0.494	4.023
UDI1(1)	46.0375	13.253	149.28	0.982	0.061	0.06	0.15	0.073	0.154	0.29	0.899	−0.301	0.051	0.315	0.123	0.148	0.128	0.37	0.969	0.712	0.22	1.179	0.534	0.221	0.549	0.384	4.237
UNPG(1)	43.1194	12.3557	350.971	1.491	0.03	0.438	0.049	0.246	0.046	0.739	1.208	−0.371	0.026	0.898	0.043	0.123	0.041	1.002	1.486	1.371	0.114	0.054	0.187	0.418	0.178	0.832	5.217
UNTR(1)	42.5587	12.6738	219.226	0.36	0.043	0.903	0.106	0.221	0.1	0.98	2.223	0.139	0.038	0.509	0.092	0.235	0.087	0.839	1.679	0.792	0.164	2.28	0.403	0.494	0.379	0.539	4.61
UNUB(1)	43.7005	12.6402	380.536	1.977	0.181	1.859	0.362	0.268	0.295	0.444	1.252	0.906	0.153	1.769	0.316	0.413	0.255	0.563	1.369	−0.257	0.686	4.518	1.375	0.347	1.121	0.465	4.995
UNUD(1)	46.0831	13.2165	179.627	0.206	0.181	1.51	0.215	0.339	0.214	0.362	1.136	−0.398	0.155	0.657	0.182	0.376	0.183	0.474	1.273	0.855	0.661	3.921	0.782	2.277	0.778	0.511	5.832
UPAD(1)	45.4067	11.8779	84.036	1.496	0.057	0.734	0.113	0.527	0.11	0.473	1.217	0.901	0.048	1.353	0.095	0.535	0.093	0.643	1.39	−1.708	0.214	3.332	0.432	0.774	0.418	0.51	4.976
UPG2(1)	43.1191	12.3558	351.176	1.174	0.135	0.182	0.142	0.246	0.13	0.406	0.952	−0.002	0.117	1.514	0.122	0.119	0.113	0.537	1.098	−0.876	0.513	2.203	0.537	1.189	0.495	0.565	5.07
VARZ(1)	44.8233	9.19741	469.377	−0.362	0.034	0.327	0.103	0.185	0.099	0.497	1.101	0.104	0.029	0.716	0.087	0.141	0.084	0.561	1.062	0.306	0.127	0.956	0.385	0.459	0.366	0.535	4.437
VEAR(1)	45.438	12.3578	46.773	0.985	0.073	1.074	0.212	0.073	0.208	0.252	0.914	−0.036	0.064	0.927	0.178	0.258	0.176	0.306	0.952	−2.865	0.304	6.702	0.864	0.263	0.846	0.352	5.305
VENE(1)	45.437	12.332	67.131	1.908	0.027	2.21	0.046	0.784	0.044	0.98	1.7	0.574	0.024	2.227	0.04	0.543	0.037	0.872	1.282	−0.455	0.106	2.844	0.179	1.203	0.169	1.28	9.507
VERC(1)	45.3313	8.42105	184.032	−0.719	0.321	0.487	0.264	0.316	0.244	0.344	0.923	−0.514	0.273	0.62	0.224	0.345	0.207	0.502	1.147	−0.152	1.163	1.135	0.97	1.313	0.89	0.371	3.642
VERO(1)	45.4447	11.0024	123.861	−0.461	0.141	1.803	0.168	0.444	0.167	0.49	1.209	0.332	0.121	1.159	0.143	0.179	0.144	0.467	0.995	−0.962	0.517	1.922	0.618	0.877	0.612	0.473	4.303
VIGE(1)	45.3148	8.86194	168.607	−0.836	0.878	0.398	0.434	0.56	0.437	0.34	1.105	0.063	0.765	1.237	0.373	0.175	0.378	0.449	1.256	0.112	3.161	2.48	1.573	2.379	1.581	0.379	4.439
VIGX(1)	45.3148	8.86196	168.678	−0.825	0.031	0.069	0.096	0.138	0.093	0.393	0.832	0.21	0.026	0.037	0.08	0.081	0.078	0.512	0.923	−0.715	0.116	0.998	0.356	0.556	0.344	0.537	4.243
VITE(1)	42.4176	12.1195	453.88	0.832	0.585	0.686	0.266	0.147	0.193	0.351	0.913	−1.422	0.537	0.29	0.242	0.111	0.173	0.541	1.274	0.227	2.207	1.244	1.002	0.676	0.724	0.435	4.262
VLCH(1)	46.607	13.8505	572.039	−0.173	0.023	1.321	0.089	0.124	0.088	0.495	1.298	0.112	0.019	0.877	0.075	0.199	0.074	0.576	1.271	0.611	0.082	1.585	0.323	0.348	0.317	0.552	5.158
VOLT(1)	45.3846	11.9109	53.396	0.825	0.02	0.582	0.087	0.136	0.084	0.362	0.795	−0.245	0.017	0.53	0.073	0.121	0.07	0.449	0.83	−0.059	0.075	1.476	0.319	0.38	0.307	0.682	5.501
ZIMJ(1)	46.8771	7.4651	954.3	−0.62	0.011	0.923	0.071	0.13	0.07	0.625	1.466	−0.074	0.009	0.987	0.059	0.204	0.059	0.78	1.552	0.392	0.038	0.713	0.257	0.715	0.253	0.667	5.691
ZIMM(1)	46.8771	7.46527	956.327	−0.795	0.075	0.47	0.12	0.422	0.119	0.665	1.313	−0.092	0.067	0.844	0.109	0.852	0.108	0.715	1.282	−1.716	0.287	1.022	0.461	1.2	0.452	0.722	5.396
ZOUF(1)	46.5572	12.9736	1946.48	−0.422	0.022	0.467	0.094	0.377	0.094	0.502	1.31	−0.115	0.019	0.924	0.078	0.363	0.078	0.531	1.151	2.516	0.08	0.843	0.332	0.41	0.333	0.527	4.842
APPI(3R)	43.353	13.3295	293.199	1.56	1.205	0	0	0	0	0.359	1.396	1.881	1.068	0	0	0	0	0.367	1.266	0.189	4.721	0	0	0	0	0.371	5.758
AULL(2R)	44.2089	9.97294	190.576	−0.589	0.083	0	0	0	0	0.619	1.653	0.21	0.072	0	0	0	0	0.67	1.576	−1.982	0.306	0	0	0	0	0.502	4.954
BDGN(3R)	44.3865	10.0304	1529.14	−0.871	0.268	0	0	0	0	1.243	2.999	−0.827	0.233	0	0	0	0	0.699	1.498	3.074	1.053	0	0	0	0	0.607	5.844

Table 1. (continued)

Site Information				North Component								East Component (mm/a)								Vertical Component (mm/a)							
Site Name[b]	Latitude	Longitude	Height (m)	V (mm/a)	σ (mm/a)	A (mm)	σ (mm)	SA (mm)	σ (mm)	NRMS	WRMS (mm)	V (mm/a)	σ (mm/a)	A (mm)	σ (mm)	SA (mm)	σ (mm)	NRMS	WRMS (mm)	V (mm/a)	σ (mm/a)	A (mm)	σ (mm)	SA (mm)	σ (mm)	NRMS	WRMS (mm)
BOBB(3R)	44.7729	9.44802	1019.53	−0.19	0.15	0	0	0	0	0.672	1.682	−1.051	0.129	0	0	0	0	0.568	1.752	2.604	0.559	0	0	0	0	1.051	8.997
CCRO(3R)	43.0785	12.854	964.951	1.071	0.11	0	0	0	0	1.448	4.216	0.854	0.094	0	0	0	0	1.978	4.912	−2.647	0.422	0	0	0	0	1.663	18.738
CDLG(3R)	43.1277	12.0556	379.363	1.933	0.114	0	0	0	0	1.788	4.27	−0.649	0.126	0	0	0	0	1.3	3.284	0.327	0.426	0	0	0	0	0.965	8.754
CDRC(3R)	44.2004	10.8618	665.066	−1.863	0.362	0	0	0	0	0.938	2.133	0.518	0.311	0	0	0	0	0.71	1.356	−1.791	1.363	0	0	0	0	0.675	5.666
CERV(2R)	44.0392	10.2463	1203.64	0.005	0.128	0	0	0	0	0.517	1.743	0.65	0.111	0	0	0	0	0.387	1.232	−0.37	0.476	0	0	0	0	0.517	6.375
CITO(3R)	43.3238	13.106	892.664	1.183	0.607	0	0	0	0	1.056	2.793	0.247	0.517	0	0	0	0	1.265	2.809	5.736	2.258	0	0	0	0	0.647	6.369
CREM(3R)	45.1351	10.0283	113.425	0.343	0.283	0	0	0	0	1.737	3.627	−0.427	0.239	0	0	0	0	1.397	2.49	−0.734	1.05	0	0	0	0	0.956	7.428
CSAN(3R)	43.0619	13.1645	878.643	2.877	0.296	0	0	0	0	1.168	3.622	0.442	0.244	0	0	0	0	0.898	2.372	−2.669	1.301	0	0	0	0	1.039	11.217
DANN(2R)	43.3956	13.145	672.139	2.429	0.37	0	0	0	0	0.52	1.744	2.339	0.327	0	0	0	0	0.704	2.102	−5.945	1.427	0	0	0	0	0.556	7.24
FRAS(3R)	43.3944	12.9595	837.027	1.793	0.546	0	0	0	0	0.756	2.182	0.621	0.476	0	0	0	0	0.742	1.905	1.222	2.027	0	0	0	0	1.398	14.993
GESS(2R)	44.4386	11.3857	295.91	−0.291	0.129	0	0	0	0	0.465	1.379	0.997	0.111	0	0	0	0	0.447	1.129	0.527	0.479	0	0	0	0	0.489	5.427
LEON(3R)	43.5787	12.5426	614.515	0.439	0.49	0	0	0	0	2.128	5.459	0.169	0.419	0	0	0	0	1.159	2.802	0.249	1.837	0	0	0	0	1.229	12.605
LUCA(3R)	43.5996	11.1176	482.612	1.083	0.464	0	0	0	0	0.843	2.371	−0.219	0.405	0	0	0	0	0.862	2.126	−2.599	1.746	0	0	0	0	0.616	6.46
LVG2(3R)	44.3338	11.3238	513.492	0.294	0.569	0	0	0	0	0.876	2.33	0.668	0.478	0	0	0	0	0.807	1.781	5.607	2.046	0	0	0	0	0.785	7.868
MACU(2R)	43.5831	13.5475	186.169	0.559	0.216	0	0	0	0	0.739	1.903	2.334	0.188	0	0	0	0	0.639	1.438	0.565	0.815	0	0	0	0	0.482	4.709
MASC(2R)	44.0329	10.1461	208.732	−0.623	0.263	0	0	0	0	0.467	1.294	−0.462	0.224	0	0	0	0	0.578	1.34	0.352	1.032	0	0	0	0	0.622	6.404
MODE(3R)	44.6317	10.9453	94.743	1.529	0.094	0	0	0	0	0.726	1.673	1.05	0.112	0	0	0	0	0.956	2.171	1.377	0.345	0	0	0	0	0.768	6.426
MPEN(3R)	43.1014	12.8888	1618.53	2.486	0.347	0	0	0	0	0.951	3.309	1.164	0.283	0	0	0	0	0.645	1.73	−5.293	1.351	0	0	0	0	1.333	17.377
MTES(3R)	44.5658	10.4521	730.234	1.401	0.184	0	0	0	0	1.517	3.865	0.316	0.162	0	0	0	0	0.658	1.387	−0.633	0.7	0	0	0	0	0.709	5.075
MVGL(3R)	44.4678	11.0906	325.376	6.325	0.814	0	0	0	0	0.3	0.652	0.627	0.687	0	0	0	0	0.538	0.981	2.596	2.917	0	0	0	0	0.675	5.293
PIAC(3R)	45.0524	9.69277	136.573	1.059	0.531	0	0	0	0	0.541	2.685	0.094	0.452	0	0	0	0	0.767	3.287	−6.64	2.029	0	0	0	0	0.406	6.84
PIET(3R)	43.6526	12.6948	620.027	−0.205	0.51	0	0	0	0	0.561	1.464	1.263	0.444	0	0	0	0	0.571	1.273	1.548	1.944	0	0	0	0	0.962	9.395
RMAL(3R)	44.3873	10.9479	607.366	2.231	0.299	0	0	0	0	0.447	0.998	0.062	0.257	0	0	0	0	0.947	1.808	1.692	1.119	0	0	0	0	0.687	5.749
RNDP(3R)	43.8873	11.8057	1136.53	1.621	0.418	0	0	0	0	0.736	3.496	−0.806	0.338	0	0	0	0	0.64	2.49	0.194	1.648	0	0	0	0	0.619	11.462
ROCC(2R)	44.3661	11.2738	514.909	2.428	0.224	0	0	0	0	0.527	1.465	0.826	0.192	0	0	0	0	0.574	1.391	4.495	0.831	0	0	0	0	0.807	8.431
SMNT(3R)	44.2203	11.3982	867.805	2.116	0.193	0	0	0	0	0.94	1.839	−0.7	0.164	0	0	0	0	0.71	1.195	−3.112	0.716	0	0	0	0	1.501	10.991
SRGF(2R)	44.1785	10.3319	781.889	−0.797	0.127	0	0	0	0	0.674	1.731	−0.065	0.112	0	0	0	0	0.818	1.862	−0.795	0.475	0	0	0	0	0.63	6.079
UCCE(3R)	43.9162	11.8527	751.276	0.72	0.391	0	0	0	0	0.438	2.81	0.569	0.31	0	0	0	0	0.584	3.122	−3.464	1.583	0	0	0	0	0.469	11
BASO(3C)	45.6429	13.875	445.88	2.099	0.273	0	0	0	0	1.161	4.545	0.132	0.226	0	0	0	0	1.248	4.165	2.858	1.016	0	0	0	0	1.871	27.207
BLEG(3C)	46.1648	14.1135	1610.91	0.888	0.193	0	0	0	0	0.521	1.385	0.582	0.158	0	0	0	0	1.077	2.336	−2.264	0.72	0	0	0	0	0.323	3.251
KOPE(3C)	45.5482	13.7241	45.979	1.324	0.163	0	0	0	0	1.444	3.834	−0.084	0.135	0	0	0	0	0.894	1.977	−0.943	0.63	0	0	0	0	0.982	10.538
MAJA(3C)	45.5038	13.6434	323.178	−0.129	0.163	0	0	0	0	1.922	5.012	−0.216	0.134	0	0	0	0	1.399	2.984	−2.115	0.614	0	0	0	0	0.477	4.758
PULM(3C)	44.8655	13.8462	80.558	1.458	0.342	0	0	0	0	0.438	1.773	0.584	0.28	0	0	0	0	0.499	1.705	1.336	1.301	0	0	0	0	0.304	4.951
RINJ(3C)	45.084	13.6294	53.608	1.335	0.261	0	0	0	0	0.313	1.144	0.939	0.223	0	0	0	0	0.396	1.254	−0.506	1.026	0	0	0	0	0.322	4.673

[a]Abbreviations: Height = height above the reference ellipsoid, s = standard error, A and SA = amplitudes of the annual and semiannual components of the time series, NRMS = normalized root-mean-squared deviation, WRMS = weighted root-mean-squared deviation.

[b]Numbers in parentheses indicate (1) Continuously operating station, (2) semi-continuous operation, (3) campaign operation. (R) indicates RETREAT GPS network, (C) indicates CRODYN GPS network.

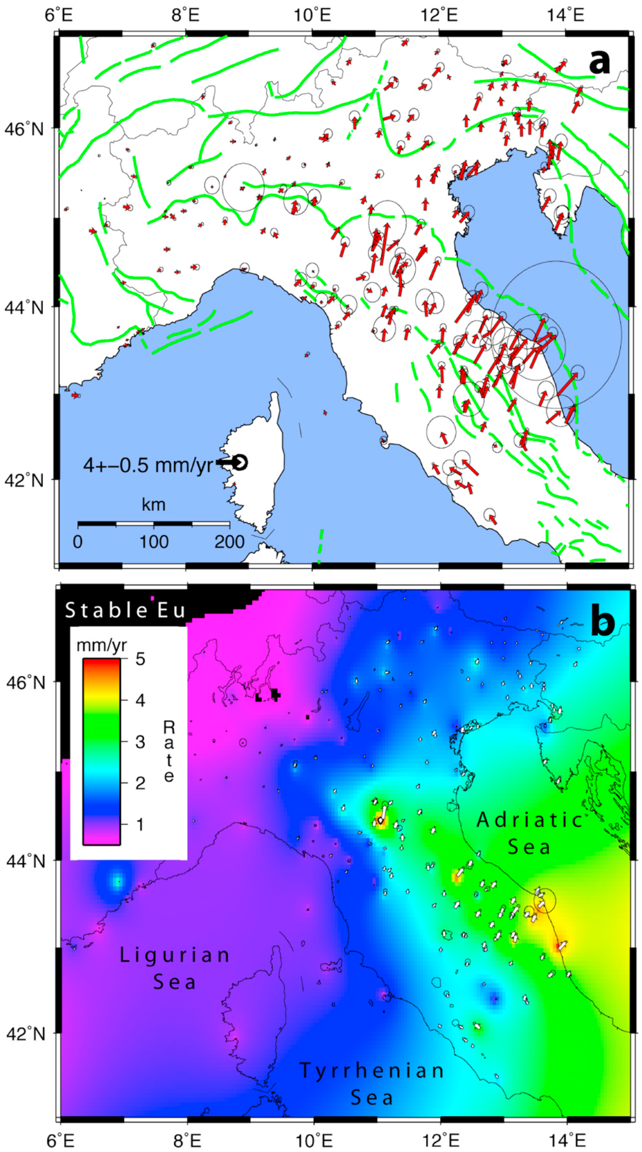

Figure 6. (a) Estimates for horizontal velocity (red vectors) from analysis described in the main text. Velocity reference frame is fixed to the stable interior of the Eurasia plate. Error ellipses represent 95% confidence regions. Green lines represent mapped faults as in Figure 1. (b) Color contours of a smoothing spline fit to the rates of motion. The black region indicates rates <0.5 mm/yr, which we here adopt as an ad hoc indication of the stable interior region of the Eurasia plate. Vectors are shown at a reduced scale relative to Figure 6a, and are plotted to give some indication of where the spline fit was constrained by actual observations. Interpolated rates are poorly constrained over the marine regions—including the Ligurian, Tyrrhenian, and Adriatic Seas—where there are no GPS stations. We present this contour map simply to illustrate that the fastest rates relative to Eurasia within our study region are found along the frontal portion of the northern Apennines orogen. The interpolated rates are not used elsewhere in our interpretations.

Bennett, 2009; *Buble et al.*, 2010; *Velasco et al.*, 2010], with the exception that here we include periodic terms in the common-mode model. The amplitudes of the north, east, and vertical annual signals are contoured in Figure 8 along with the distribution of WRMS scatter in the north, east, and vertical coordinate components.

[26] Differences between the velocity estimates based on the pre-filtered time series and CSC velocity estimates are zero for the continuous stations. This is because periodic site motions were included in the kinematic models used to estimate the pre-filtered results, CMS, and CSR velocities. Differences between the various velocity estimates for the campaign GPS stations are nonzero, but statistically insignificant. Small differences arise because periodic motions were not part of the kinematic models used to estimate pre-filtered and CSR velocities for these stations, whereas the CSR time series were corrected for CMS periodic motions (derived from the continuous stations). These differences are small because of the small amplitude (<0.5 mm horizontal, <3 mm vertical) of the seasonal terms (Table 1) and also owing to our campaign strategy, which involved multiyear observations during the same season each year. Due to the limited temporal sampling of campaign GPS measurements, we could not estimate the total periodic site motion for these stations. We rely on our observation strategy to mitigate the effect of possible site-specific periodic motion for campaign sites. We discuss the amplitudes of the spatially variable components of the continuous stations in more detail below.

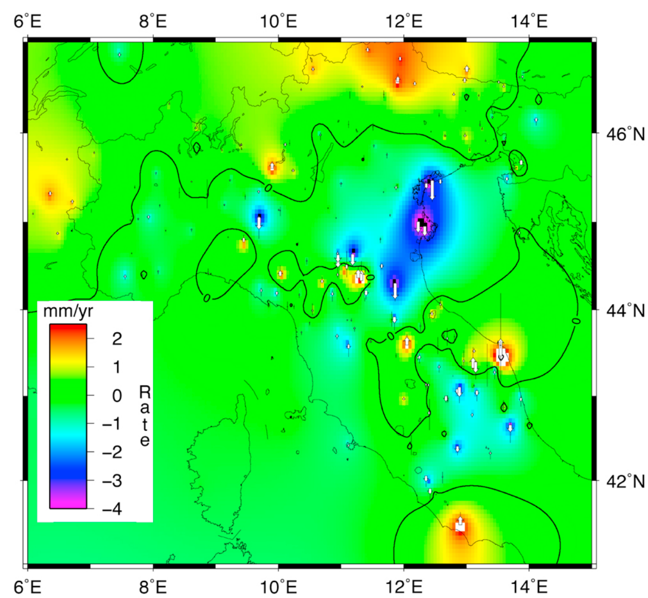

Figure 7. Vertical velocity estimates derived from CSR time series. White vectors show vertical rates with error bars representing 2-σ confidence regions. The color contour represents a smoothed spline model fit to the estimated rates. In general, uplift (positive vertical rate) appears to occur within the northern Apennines and Alps orogens, whereas subsidence (negativevertical rate) occurs primarily in the Po Plain, particularly along the coastal portion of the Po Plain. The apparently isolated uplift at latitude 41.5°N could be associated with a volcanic source.

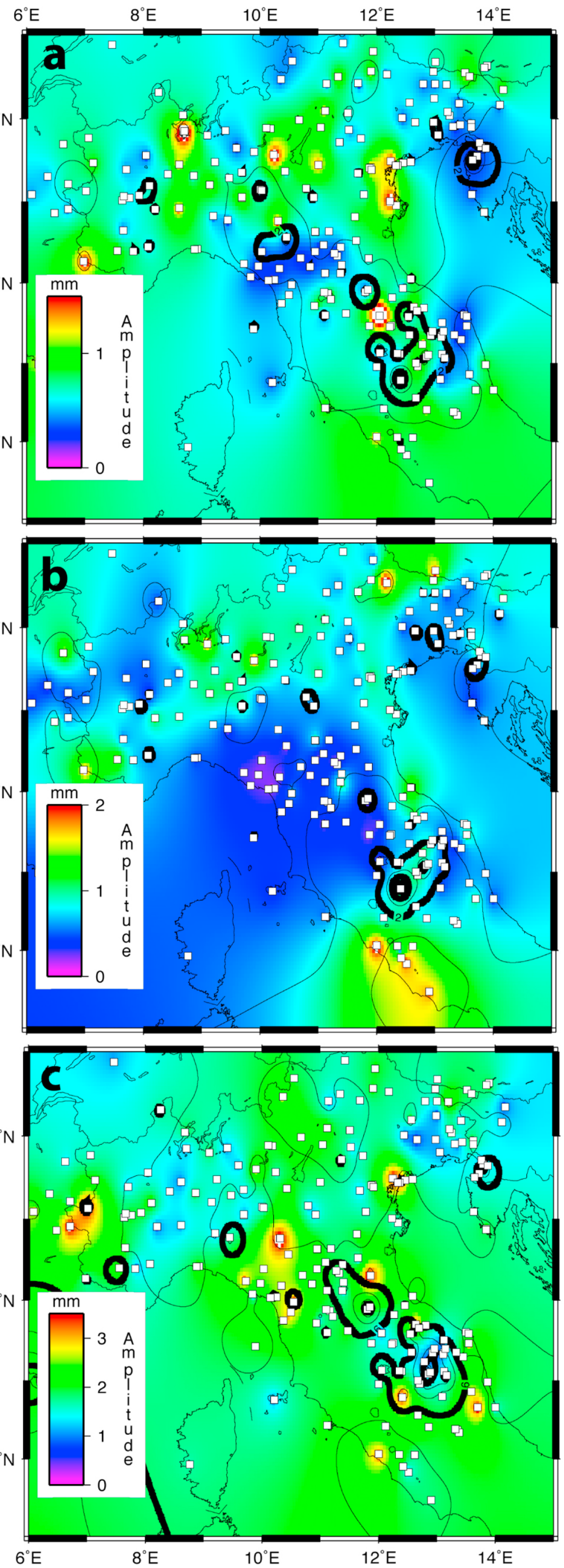

Figure 8. Color contours of the amplitude of annual site motions for each coordinate component versus line contours of WRMS scatter for the same components. Contours are derived from smoothing spline fits to the amplitude and WRMS values at each site. (a) North components. Thick black line contours for WRMS at 2 mm increments. (b) East components. Thick black line contours for WRMS at 2 mm increments. (c) Vertical components. Thick black line contours for WRMS at 3 mm increments.

[27] The horizontal CSR velocities show significant variations in the style and amount of crustal motion across northern Italy (Figure 6). In general, velocities west of about 10°E longitude are less than 1 mm/yr, decreasing with increasing distance to the north and west toward the interior of the Eurasia plate (Figure 6b). Velocities to the east of 10°E longitude are generally greater than 1 mm/yr. The largest rates, >4 mm/yr, are observed at sites within the northern Apennines (Figure 6b). Velocities for Istria, Croatia, which is within the rigid interior of the Northern Adria microplate [e.g., *Weber et al.*, 2010] are about 3 mm/yr (Figure 6b), somewhat lower than velocities in the northern Apennines. At the 45°N parallel, there is an abrupt decrease in velocity between the 11 to 12°E meridians (Figure 6b). This decrease indicates NE-SW horizontal shortening coinciding with the ARF (Figures 1 and 6a), which is a zone dominated by thrust-sense seismicity (Figure 3).

[28] The vertical CSR velocities (in the no-net-vertical velocity reference frame) are shown in Figure 7. The most striking feature of the vertical velocity field is the general absence of long-wavelength variations. Most stations have small vertical motions ($|V_u| < 1$ mm/yr) (Table 1), but there are a few prominent exceptions. The largest vertical velocities are in the eastern Po Plain region, along the Adriatic coast (Figure 7). Stations in this location reveal subsidence at rates in excess of 3 mm/yr. These estimates are consistent with rates inferred independently by *Baldi et al.* [2009]. This motion is probably related to long-term subsidence given that it appears to be independent of local cities (which pump groundwater) and is observed over a distances in excess of 100 km. Long-term subsidence could be caused by loading associated with rapid sedimentation [*Bertotti et al.*, 1997; *Picotti and Pazzaglia*, 2008; *Carminati et al.*, 2003a], or could represent a flexural response to slab sinking [*Carminati et al.*, 2003b]. Uplift exceeding 1 mm/yr is observed along the northern Apennines orogen, and at various locations within the Alps. The broadest and most spatially coherent uplift anomaly occurs in the eastern Alps at 12°E longitude. Vertical rates are generally quite small in coastal regions, consistent with the findings of *Bennett and Hreinsdóttir* [2007] and *Buble et al.* [2010].

[29] Figure 8 shows contour maps of the CSR-based estimates for the amplitudes of annual site motion in all three coordinate components. Also shown in Figure 8 are contours of the WRMS scatters of site motion for the respective coordinate components. Figure 8 shows that there is little, if any, correlation between annual site motion and long-term variance in site velocities. *Langbein* [2008] observed marginally significant correlations between annual motions and long-term noise statistics for continuous GPS networks

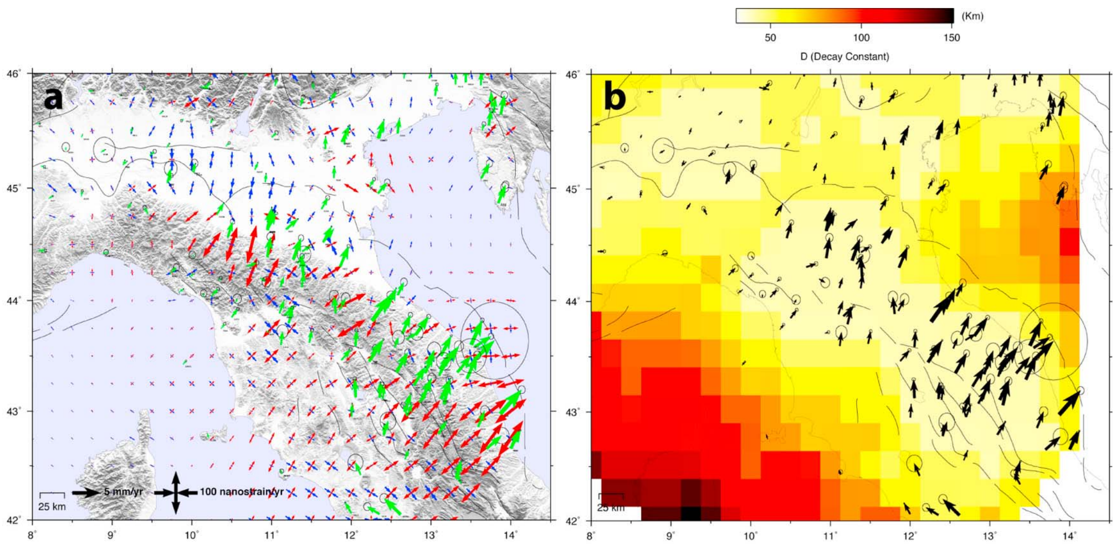

Figure 9. Strain rate field inferred from GPS velocities using method described by *Shen et al.* [1996]. Red indicates extension, blue indicates shortening, and green arrows represent the velocity data from which the strain rate field was derived.

in southern California. We find no apparent correlation between seasonal site motions and scatter, suggesting that seasonal perturbations to site motion are adequately accounted for in our time series analysis. By visual inspection of the residual time series, we also find no evidence for non-periodic transients in the coordinate time series, although it is possible that more sophisticated methods for identifying transient signals in GPS time series might reveal signals that are difficult to discriminate by visual inspection.

[30] The NRMS values for the horizontal components of the common-mode noise process are near one, indicating scatter at a level consistent with the uncertainty estimates. However, the NRMS value for the vertical component of the common-mode noise is 2.6, indicating scatter that is larger than expected based on the uncertainty estimates. The WRMS scatter of the horizontal components is 0.3 mm, significantly smaller (<30%) than the WRMS misfits of the kinematic model to the CSR time series. These results indicate that the common-mode noise does not contribute appreciably to the total error budget for horizontal components. In contrast, the WRMS scatter of the vertical component of the common-mode noise process is 2.9 mm/yr, which is >50% of the scatter associated with most of the continuous GPS stations.

[31] We find a very small common-mode periodic site motion in the horizontal components. Amplitudes of the annual components of the common-mode seasonal motion are 0.167 ± 0.008 mm and 0.124 ± 0.007 mm for the north and east, respectively. Amplitudes of the semi-annual components of the common-mode seasonal site motion are even smaller, 0.008 ± 0.008 mm and 0.038 ± 0.007 mm for north and east, respectively. The amplitudes for common-mode annual and semi-annual for the vertical component are 2.55 ± 0.03 mm and 0.54 ± 0.03 mm, respectively. For comparison, amplitudes of the site-specific component of annual motion exceed 2 mm in the horizontal components and 3 mm in the vertical.

5.2. Strain Rate Analysis

[32] We use the estimated CSR horizontal velocities to invert for the velocity gradient tensor field. We use the approach described by *Shen et al.* [1996], which accounts for velocity uncertainties, network geometry and inter-station distances. Strain and rotation rates are estimated on a regular 0.25° grid using the velocity data accounting for their uncertainties by weighted least squares. The grid representing the model domain extends between longitude 7° and 15°E and latitude 41° and 47°N. Each velocity data point was re-weighted by a Gaussian function $\exp(-\Delta R^2/D^2)$, where ΔR represents the distance between the geodetic station associated with the data point and the grid point at which strain is to be evaluated. D is a smoothing parameter that is optimally determined, for each node of the regular grid, through balancing the trade-off between the formal strain rate uncertainty estimate and the total weight assigned to the data (cf. *Shen et al.* [2007] for more details). According to this weighting scheme, measurements made closer to a grid point contribute more to the strain rate estimate at that point, and the smoothing is applied according to the station distribution and density. The re-weighting determines the degree of smoothing around a given spot and the uncertainties of the strain estimates, while the D value can be considered as an indicator of how local or regional the strain rate tensor inverted at each grid point is. Adopting this approach to estimate the strain rate field from horizontal velocities in Figure 6a, we obtain D values ranging between 30 and 150 km (Figure 9); most values indicate that our strain rate field is resolved at spatial wavelengths longer than about 50 km.

[33] The estimated strain rate field is shown in Figure 9. Within and west of the northern Apennines, where the strain rate field is well resolved, the deformation field is dominated by extensional strain. The largest rates of extensional strain are observed near the crest of the range. To the northeast of the orogen, in the Po Plain and eastern Alps, the deformation

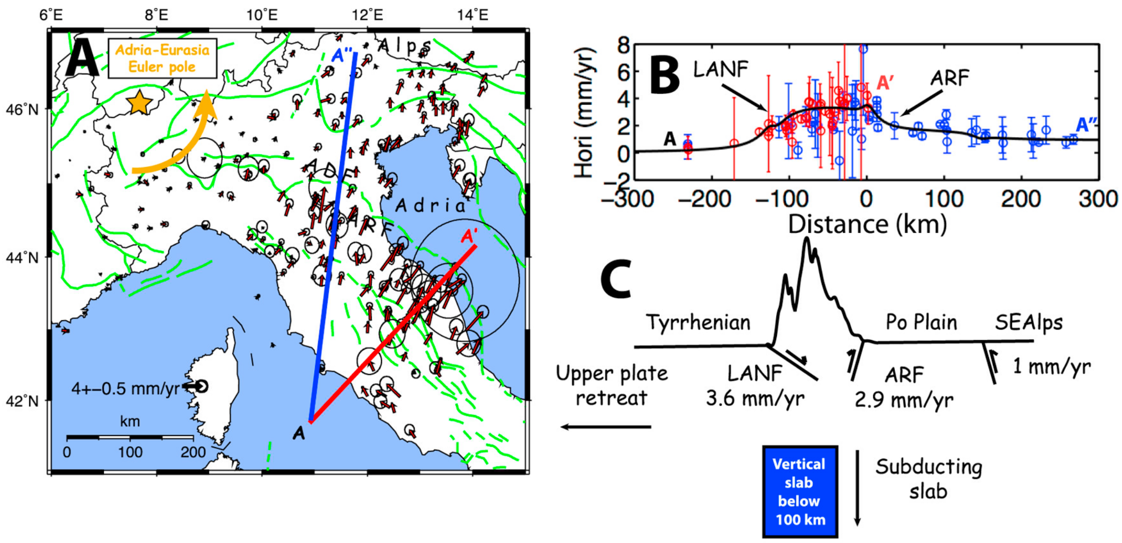

Figure 10. (a) Location of two velocity profiles (A-A′ and A-A″) representing different segments of the northern Apennines. The southern profile (A-A′) crosses the northern Apennines orogen at the latitude where potential present-day shortening is predominantly offshore, and onshore strain accumulation is dominated by extension. The northern profile (A-A″) crosses the northern Apennines orogen, the Po Plain, and Eastern Alps, recording shortening across the ARF and eastern Alps deformation front, but not the ADF. The general location of the Adria-Eurasia Euler pole is represented by a gold star. Adria rotates counter clockwise relative to the Eurasia plate as indicated by the golden arcuate arrow. (b) Profile parallel components of horizontal velocities for sites within 50 km of profile A-A′ (red) and profile A-A″ (blue), respectively. Error bars represent 1-σ uncertainties. Extensional strain is apparent in the horizontal data for both profiles between the Tyrrhenian and northern Apennines, as indicated by an increase in northeast-directed velocity with northeast distance along the profile (orthogonal to the range). Shortening is apparent between the northern Apennines and Po Plain. A smaller amount of shortening (totaling ~1 mm/yr across a distance of ~50 km) is also apparent between the Po Plain and the eastern Alps. There is no signal apparent at the location of the ADF. The solid black curve overlying the data points, representing a simple model for crustal velocity calculated using three buried edge dislocations in an elastic halfspace, reproduces the 1st order features of the velocity profile. (c) Schematic diagram showing the relationship between Apennines topography, inferred crustal faults, and the Apennines slab, which is imaged tomographically at depths between about 100 to 300 km depth.

field is dominated by crustal shortening. The largest rates of shortening are imaged in the central part of the Po Plain. The amplitudes of strain rate for both shortening and extension are less than 100 nanostrain/yr, which is typical of diffusely deforming continental plate boundary zones (e.g., the Basin and Range Province, the Tibetan plateau) [e.g., *Kreemer et al.*, 2003].

6. Discussion

6.1. Crusal Velocity and Strain Rate Pattern

[34] Our GPS velocity estimates provide a new, detailed view of the active deformation within the northern Apennines and adjacent areas. We find general consistency between the strain rate field we have inferred from GPS velocities and the strain rate field of *Barani et al.* [2010], which is based on the tensor summation of earthquake focal mechanisms. Our velocity estimates are also consistent with previous inferences on Adria microplate motion based on sparse GPS [*Calais et al.*, 2002; *Battaglia et al.*, 2004; *Serpelloni et al.*, 2005], and/or earthquake focal mechanism data [*Anderson and Jackson*, 1987; *D'Agostino et al.*, 2008; *Weber et al.*, 2010]. The advantages of the GPS method for determining the strain rate field relative to inferences based on focal mechanisms are that (1) GPS strain rate estimates are not restricted to seismogenic zones, and (2) GPS records the complete instantaneous strain rate field, including (ephemeral) elastic and aseismic strain components of crustal strain accumulation. GPS measurements of active crustal velocity also directly record relative motions among non- or slowly deforming microplates, which can only be inferred indirectly from the focal mechanisms of earthquakes that occurred within the deforming margins of the microplates.

[35] One consideration when interpreting strain rate estimates derived from point measurements of crustal velocity is the inherent non-uniqueness of the strain rate estimation problem. The resolution of strain rate fields inferred from the discrete set of GPS velocity estimates is necessarily limited by the distribution of stations, and observational errors [e.g., *Baxter et al.*, 2011]. Strain rate estimates derived from geodetic data may be thought of as spatially smoothed, low-pass filtered versions of the true strain rate field, such that some short-wavelength features of the true field may not be apparent in the estimated field. Despite

such limitations, our strain rate model (Figure 9) clearly reveals a marked transition from horizontal extension to horizontal shortening across the Apennine Range front (ARF) that is not likely to be an artifact of the strain rate estimation procedure.

[36] To further explore the details of this strain rate transition, we project the velocity data onto profiles orthogonal to the strike of the Apennines range (Figure 10). The profiles have been constructed in an attempt to account for the two-dimensional nature of the horizontal velocity field. Because deformation in and around the northern Apennines is kinematically linked to the motion of the northern Adria microplate, which rotates rapidly counterclockwise relative to Eurasia about a pole located in the southwestern Alps [e.g., *D'Agostino et al.*, 2008; *Weber et al.*, 2010], velocities depend strongly on the azimuth of the GPS stations' locations relative to the Euler pole location. Consequently, stations immediately east of the pole tend to be directed northward, and stations immediately south of the pole tend to be directed eastward. We accounted for this effect by projecting data onto two profiles locally oriented perpendicular to the range crest (Figure 10a). The independent profiles are plotted relative to a common abscissa, by shifting the x-axes so as to align the projected data to a common origin relative to the crest of the range (Figure 10b). In forming this one-dimensional representation of the two-dimensional velocity field, we made no attempt to adjust for systematic increases in rate with distance from the northern Adria Euler pole. The similarity of the rate profiles after alignment in terms of overall pattern and amplitude of motion (Figure 10b) suggests that this latter effect is of second order.

[37] The composite velocity profile (Figure 10b) generally supports inferences derived from the two-dimensional horizontal strain rate field (Figure 9). To the west of the Apennines crest, we observe a northeast-directed velocity gradient. Rates increase toward the northeast across the network, indicating extensional strain accumulation. A maximum rate of $\sim$4 mm/yr is observed near the crest of the range. To the northeast of the crest, velocities decrease rapidly across the ARF. A smaller, but nevertheless significant, drop in velocities occurs across the front of the eastern Alps. These decreases in the northeast components of velocity with northeast distance clearly indicate shortening there. The relatively steeper slope of the velocity gradient associated with the shortening ($\sim$3 mm/yr over $\sim$60 km) as compared to that associated with the extending portion of the range ($\sim$4 mm/yr over $\sim$180 km) implies roughly a factor of two difference between horizontal shortening and extension rates (50 versus 22 nanostrain/yr, respectively). The net velocity difference across the Apennines range, which represents motion of Adria relative to Eurasia (including Corsica and Sardinia), indicates net divergence of nearly 2 mm/yr, consistent with previous inferences [e.g., *Stein and Sella*, 2006].

[38] Vertical velocities inferred from our analysis are generally consistent with the recent study of *Baldi et al.* [2009], which was based on a subset of the data set of the continuous GPS stations considered here, with broad subsidence in the Po Plain and uplift in the Apennines and eastern Alps. However, our study clearly reveals small but systematic uplift of mountainous regions not apparent in the Baldi et al. study.

[39] The new crustal motion data set that we present here clearly reveals active shortening along the Apennines range front. This result is consistent with the distribution of thrust-sense earthquakes, which tend to be located along the external front of the range (Figure 3). Hypocenters of instrumentally recorded earthquakes show that thrust events extend to great depths beneath the range, with focal mechanisms that are consistent with a steeply southwest-dipping thrust plane (Figure 3). The narrow width ($\sim$60 km) of the zone of crustal shortening, coupled with the observed uplift of the Apennines crest relative to the Po Plain is also compatible with deformation being controlled by a steeply dipping structure; a shallow dipping fault might produce a broader distribution of deformation and a lower ratio of vertical to horizontal motion across the range front. This inference based on crustal velocities agrees well with the geomorphologic studies of *Picotti and Pazzaglia* [2008] and *Benedetti et al.* [2003].

6.2. Implications for Crustal Deformation

[40] To further explore the implications of the GPS measurements for crustal deformation mechanisms, we forward modeled the velocity profile data in Figure 10 assuming three crustal faults, representing a low angle normal fault (LANF) bounding the western range front of the northern Apennines, a steep dipping reverse fault representing the Apennines Range Front (ARF) fault, and a steep dipping reverse fault bounding the southeastern Alps (Figure 10b). The parameters describing the Apennine bounding model faults are based loosely on the previous work of *Hreinsdóttir and Bennett* [2009] and *Picotti and Pazzaglia* [2008]. To model the crustal strain associated with all three faults, we used expressions for an edge dislocation embedded in an elastic half-space [e.g., *Segall*, 2010]. We calculated surface velocity assuming values for dislocation location, locking depth, dip, and displacement rate. We chose the locations of the dislocation planes such that the plane would intersect the Earth's surface at the respective range front (Figure 10b). We assumed a locking depth of 12 km. We prescribed dips of 20° for the LANF, and 50° for both reverse faults. We assigned slip rates to the LANF, and the ARF and SE Alpine reverse faults of 3.6 mm/yr, 2.9 mm/yr, and 1.1 mm/yr, respectively. These slip rates were not determined by a least squares fit to the data, though they do provide a reasonable first-order fit to the data. Instead, they were based loosely on previous studies [e.g., *Benedetti et al.*, 2003; *D'Agostino et al.*, 2005; *Picotti and Pazzaglia*, 2008; *Hreinsdóttir and Bennett*, 2009] and a fit to the velocity data by eye. The goodness of fit is quantified by the WRMS misfit of the residual velocities after subtracting the forward model from the data. For the prescribed slip rates the WRMS statistic is 1.9 mm/yr and the associated variance reduction is 75%. We leave development and quantitative evaluation of more realistic deformation models, possibly including a formal inversion for fault model parameters and a numerical assessment of the possible relationships between surface motion and slab dynamics for future study.

[41] The overall consistency we find between GPS velocity estimates and a simple buried dislocation model

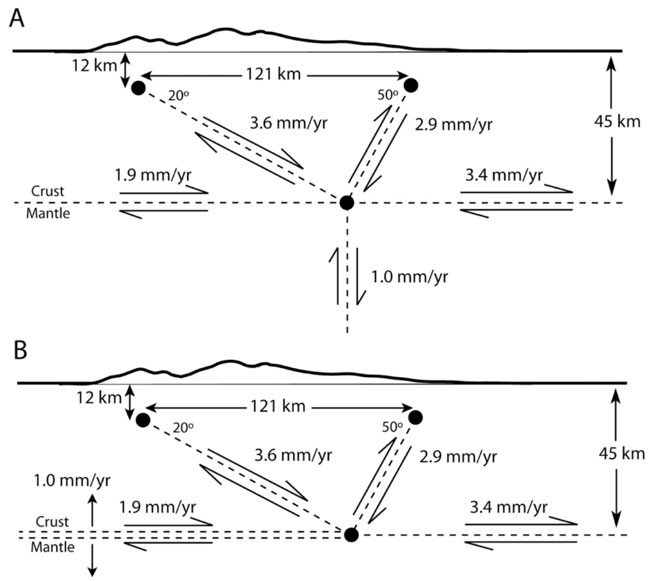

Figure 11. Numerically equivalent dislocations models illustrating the inherent non-uniqueness of the buried dislocation model. (a) Two dipping finite length dislocations with opposing dip in the mid-to lower crust meet at a depth of 45 km. Three dislocations radiate from the point intersection: two horizontal and one vertical edge dislocation. This model generates the same surface velocity profile as shown in Figure 10b, which was calculated assuming two edge dislocations of infinite extent. (b) Same as for the model depicted in Figure 11a except that the vertical edge dislocation is replaced by a horizontal tensile dislocation. Neither of the models shown in Figures 11a or 11b requires truncation of one dislocation by another.

(Figure 11b)—which was inspired by fault dips, slip sense, and slip rate based on limited existing geological and geophysical data [e.g., *Picotti and Pazzaglia*, 2008; *Hreinsdóttir and Bennett*, 2009]—is encouraging. However, several issues warrant caution when interpreting elastic dislocations models in a geodynamic context.

[42] First, Earth is not a homogeneous elastic halfspace. At the scale of our study, which spans a modest area of $\sim$250,000 km^2, encompassing northern Italy and neighboring regions, both the curvature of the Earth and vertical stratification of elastic moduli within the crust and mantle should have only second order effects that would not affect our basic conclusions [e.g., *Sun and Okubo*, 2002]. A more important consideration, however, is the extent to which inelastic behaviors contribute to the present-day deformation field as sampled by GPS geodesy. Inelastic behavior could take a number of forms falling into two broad categories: (1) viscoelastic behavior, resulting in short-term transient deformation following large earthquakes or other episodic sources of deviatoric stress change, and (2) viscoplastic behavior in the form of folding, flow, and other varieties of non-recoverable penetrative deformation.

[43] Based on the historic earthquake record, we expect negligible transient deformation associated with the viscoelastic response of the northern Apennines lithosphere to stresses induced by large earthquakes. Only one earthquake in northern Italy (1920 Garfagnana) had a magnitude greater than M6 during the past century. The smaller more recent events (e.g., 1971 M_b 5.7, 1983 M_s 5.0 Parma, 1996 M_w 5.4 Reggio Emilia, and 2003 M_w 5.3 Monghidoro) may not have been large enough to excite flow of lower crustal or upper mantle rocks sufficient to appreciably modify the secular strain rate field at the surface. Furthermore, we assume that crustal strain associated with ongoing glacial isostatic adjustment (GIA) following loss of Fennoscandian or Alpine glacial mass is negligible. Velocity gradients in northern Italy associated with Pleistocene deglaciation in distant Fennoscandia appear to generate very low strain rates at the latitude of northern Italy according to current models [e.g., *Hill et al.*, 2010]. Ongoing deformation associated with the loss of the smaller Alpine Würm glacier is expected to result in small amplitude ($<\sim$0.5 mm/yr) vertical deformation localized in the Alps [*Stocchi et al.*, 2005]. Even if post-seismic and GIA signals in the northern Apennines contribute observably to the strain rate field in the northern Apennines, they are unlikely to change the character of the deformation field enough to alter our main conclusions.

[44] The question of whether viscoplastic deformation of the northern Apennines lithosphere contributes appreciably to the contemporary deformation field on time scales of relevance to GPS geodesy is largely unknown. In seismically active plate boundary zones it is customary to model the crustal strain field assuming some combination of elastic and viscoelastic materials. These rheologies are thought to provide adequate descriptions of deformation on time scales of the order of the earthquake cycle. However, implicit to this assumption is the expectation that the steady state accumulation of strain in the crust—upon which viscoelastic transients are superimposed—represents recoverable elastic strain, which is episodically converted into localized fault displacement during discrete slip events. In many continental plate boundary zones, especially where rates of deformation are of order 10 mm/yr or larger, there appears to be general agreement between geologically inferred fault slip rates and geodetically inferred fault slip rates, suggesting that crustal strain accumulation observed geodetically is dominated by recoverable elastic strain in those locations [e.g., *Spinler et al.*, 2010]. However, where the rates of deformation are relatively low and large earthquakes occur infrequently, such as in the northern Apennines region, it is difficult to quantify how much relative plate motion is being accommodated through aseismic mechanism(s), perhaps involving diffuse, penetrative, non-recoverable strain.

[45] Literally interpreted, the model dislocation planes representing the orogen-bounding LANF and ARF reverse fault—which have opposing dips—would intersect at a depth of about 45 km assuming the dislocation geometry remains planar below the dislocation tips. Such a geometric configuration is physically untenable, because slip on one fault would lead to a step in the other fault's plane. However, it is possible to interpret the physical significance of buried dislocation models in several ways, not all of which are physically implausible.

[46] The most literal interpretation of the buried dislocation lines is that they represent fault planes or highly localized shear zones that penetrate to great depth into the Earth. Several models for lithospheric deformation consisting of a

thick elastic lithosphere dissected by discrete throughgoing faults overlying a weak asthenosphere have been discussed in the literature [e.g., *Nur and Mavko*, 1974; *Savage and Prescott*, 1978; *Thatcher and Rundle*, 1979]. Deformation below the elastic lithosphere is accommodated by viscous flow. The asthenosphere is assumed to be so weak as to impart very little shear stress to the base of the plates. So long as the lithospheric plate thickness is large relative to the burial depth of the dislocation tips in these models, stress will accumulate within the elastic lithosphere, and the system might be well approximated by the buried dislocation model [e.g., *Savage and Prescott*, 1978].

[47] However, an alternative view of lithospheric deformation is also possible. According to this alternative, fault slip rates are determined by distributed flow in the upper mantle, because the strength of the flowing upper mantle exceeds that of the overlying, relatively thin, crust [e.g., *Lamb*, 1994; *Bourne et al.*, 1998]. Discrete faults and crustal blocks are envisioned to exist only at crustal depths. In the simple dislocation model presented in Figure 10b, the point of intersecting dislocation planes at ~45 km depth might thus be interpreted as the point below which motion in the mantle lithosphere is resolved by flow, an inference supported by the fact that 45 km depth corresponds to the depth of the Adriatic Moho [*Levin et al.*, 2002]. The issue of whether the stresses arising from shallow mantle flow dominate the crustal deformation pattern is not constrained by the crustal kinematics. Nevertheless, the notion of one edge dislocation truncating another beneath the northern Apennines is obviated if we permit that the motion accommodated by discrete faulting in the crust may be resolved differently, perhaps assisted by flow, below Moho depth.

[48] The stress singularities associated with the buried dislocation tips, which drive the motion of the model halfspace surface, may be thought of as idealizations of real crustal stresses that originate from upper mantle flow. The inherent non-uniqueness of the dislocation model itself permits us to interpret these stress singularities as arising from an infinite number of possible dislocation geometries. For example, any dipping edge dislocation may be represented exactly as the sum of horizontal and vertical edge dislocations with coinciding dislocation tips, as the sum of horizontal edge and tensile dislocations, or any appropriately weighted linear combination of these idealized endmembers. Figure 11 shows two such representations that are numerically equivalent to the infinite edge dislocations used to generate the curves in Figure 10b. In these alternative geometries there is no truncation of one dislocation by another. Such representations might serve as a way to visualize the kinematics of upper mantle deformation in settings where paired belts of extension and shortening coexist in close proximity.

[49] A final issue with the interpretation of buried dislocations that requires explanation is that slip on any one of the prescribed dipping dislocation planes would result in a net far field vertical offset of the halfspace surface, requiring infinite work against gravity [e.g., *Forsyth*, 1992]. In the real Earth, the lithosphere flexes in response to gravitational forces, achieving isostatic equilibrium. The lateral distance across which crustal and upper mantle buoyancy is balanced is controlled by the effective elastic thickness of the lithosphere. The vertical components of motion predicted by the normal and thrust faults of Figure 11b are opposite in sense, such that the net vertical component of motion summed across the model fault system is small (~1 mm/yr). Thus, it might be very difficult to discriminate the details of any model accounting for flexural accommodation of vertical fault offsets unless the effective elastic thickness of the northern Apennines was very small. The halfspace model presented here may be thought of as representing an endmember flexural model with plates of very large thickness, which for the northern Apennines case, might serve as an adequate approximation to flexural models of finite elastic thickness so long as the flexural wavelength is of the order of the width of the Apennines orogen or longer, such that the long-wavelength vertical offsets from faults of opposing dip would tend to cancel.

[50] We make no attempt here to reconcile the short-term deformation field with the long-term stability of syn-convergent extension or how it is possible to develop such a configuration through a physically plausible dynamic process. We note that the pattern of present-day crustal deformation is highly consistent with the thermochronometric data set of *Fellin et al.* [2007] and *Thomson et al.* [2009], who analyzed a large set of apatite (U-Th)/He and fission track age data showing significant spatial and temporal variations in Mio-Pliocene exhumation pattern across the northern Apennines. They observed rapid late Miocene (ca. 3–5 Ma) exhumation at ~1 mm/yr on the eastern contractional side of the range, but slower exhumation of ~0.3 mm/yr within the extending central and western side of the range. A larger exhumation rate of ~1 mm/yr within the extending range core since Pliocene time (ca. 3 Ma) may be explained by either underplating or out-of-sequence shortening during continued convergence, or enhanced Pliocene uplift and erosion driven by lithospheric delamination or slab detachment [*Thomson et al.*, 2009]. Our GPS velocity estimates, which reveal ongoing shortening concentrated across the Apennines range front (ARF) well inboard of the Apennines deformation front (ADF), favors enhanced uplift driven by out-of-sequence shortening. The overall consistency between the instantaneous deformation field and the Cenozoic geology suggests that it should be possible to develop a dynamic model in which syn-convergent extension arises spontaneously as a stable configuration.

6.3. Implications for the Contemporary Geodynamics of the Northern Apennines

[51] Regardless of how present-day deformation is accommodated within the lithosphere, it is informative to consider the possible relationships between upper crustal motions and deeper mantle structure. Modern seismic tomography and receiver functions reveal a steeply dipping intact slab directly beneath the northern Apennines orogen in the latitude range 43° to 46° [e.g., *Lucente et al.*, 1999; *Wortel and Spakman*, 2000; *Piromallo and Morelli*, 2003; *Bianchi et al.*, 2010; *Benoit et al.*, 2011]. The southern boundary and depth extent of the slab are well resolved by current seismic data sets [*Benoit et al.*, 2011]. The majority of the GPS data set that we are investigating here lies directly above the region where the slab is apparent in the seismic images. The observed deformation field is consistent

with active subduction and retreat [e.g., *Waschbusch and Beaumont*, 1996] or active delamination [e.g., *Gogus and Pysklywec*, 2008] of the slab (Figure 2a). Contemporary extension within the orogen seems consistent with a model driven entirely by absolute motion of the upper plate away from a stagnant non-subducting slab (Figure 2c), but this upper plate retreat model is incompatible with the modern deformation field because there would be no crustal shortening under that scenario [e.g., *Waschbusch and Beaumont*, 1996].

[52] Orogenic extension driven by excess gravitational potential energy has been proposed as an explanation for syn-convergent extension in the northern Apennines. Excess buoyancy may derive from the replacement of a dense slab with buoyant asthenosphere following slab detachment [e.g., *Royden*, 1993; *Wortel and Spakman*, 2000; *Carminati et al.*, 1998] (Figure 2b), upwelling in the wake of a sinking slab [e.g., *Carminati et al.*, 1998], or from over-thickened crust (Figure 2d) unsupported by sufficient horizontal compressive stress [e.g., *Jolivet et al.*, 1998]. Previous authors have shown how gradients in gravitational potential energy could produce paired belts of extension and shortening under some circumstances [e.g., *Dalmayrac and Molnar*, 1981; *Platt*, 1986; *Carminati et al.*, 1998; *Gogus and Pysklywec*, 2008]. *D'Agostino et al.* [2001] associate regional uplift and Quaternary extension in the central Apennines where seismic tomography [e.g., *Benoit et al.*, 2011] reveals no slab to mantle upwelling. However, as discussed above, the detachment scenario is inconsistent with the seismically imaged slab in the northern Apennines. Thus, explanations for orogenic extension in the northern Apennines that appeal exclusively to excess buoyancy would require either a sinking slab or a crustal source. If the transition between extension and shortening is controlled entirely by changes in vertical stress between the highlands and the lowlands associated with variations in crustal thickness, it would generate a maximum resolved shear stress averaged over the thickness of the crust of less than $\sim$10 MPa assuming crustal density of 2700 kg/m^3, and a maximum elevation difference between Po plain and Apennines crest of 2 km (cf. calculations of *Dalmayrac and Molnar* [1981]). It is possible that the LANF and steep dipping reverse faults bounding the northern Apennines orogen may slip under such a low resolved shear stress due to low coefficients of friction or high pore pressures [e.g., *Collettini et al.*, 2009]. But, the pattern of deformation predicted in such a model would be symmetric, with two belts of shortening, one on either side of the orogen (Figure 2d). The absence of shortening on the southwestern side of the range along the Tyrrhenian coast would require either variations in fault friction or pore pressure, or variations in horizontal compressive stress such that σ-1 remains vertical to the southwest of the range, whereas σ-1 is horizontal to the northeast, oriented orthogonal to the range despite equivalent decreases in vertical stress relative to the highlands. Based on these considerations, the available data seem more consistent with excess buoyancy deriving from upwelling asthenosphere in the wake of a sinking, negatively buoyant slab.

[53] Although retreat of the upper plate (Figure 2c) does not provide a mechanism for crustal shortening above the slab, upper plate retreat is not exclusive of either rollback of a subducting slab or delamination of lower lithosphere. Addition of some component of upper plate retreat to a model for slab sinking would serve to increase the rate of crustal extension relative to that which would occur in association with slab rollback. Indeed, we observe net divergence between the Eurasia plate and the Northern Adria microplate across the northern Apennines (Figure 10b), as noted by several previous authors [e.g., *Anderson and Jackson*, 1987; *Calais et al.*, 2002; *Battaglia et al.*, 2004; *Serpelloni et al.*, 2005; *D'Agostino et al.*, 2008; *Weber et al.*, 2010], consistent with horizontal component of extensional deformation exceeding crustal shortening. *Waschbusch and Beaumont* [1996] showed that net divergence across an orogen is not likely to generate shortening of accreted materials as they pass from the lower plate to the upper plate. Net divergence across the orogen is not a characteristic of models that appeal to slab sinking. However, it is possible that divergence signifies some amount of upper plate retreat relative to the imaged slab, accompanied by rollback-subduction or delamination. That is, the two processes are not mutually incompatible. Qualitative support for such upper-plate retreat is provided by some (though not all) "absolute" plate motion models, but the low rates of motion implied by the current results ($\leq$4 mm/yr) do not require fast retreat (of order several mm/yr or more) as envisioned by some previous authors [e.g., *Doglioni*, 1990, 1991]. Alternatively, small-scale mantle circulation within the Mediterranean plate boundary zone, superimposed upon any possible global circulation, may provide a resistive drag on the Adria plate causing it to move roughly eastward relative to the Eurasia plate [*Panza et al.*, 2007; *Barba et al.*, 2008]. It is possible that the drag on the slab might also enhance slab rollback, contributing to the steepness of the slab.

[54] Models appealing to partial slab detachment or active slab tearing [e.g., *Wortel and Spakman*, 2000] (Figure 2b) might also be expected to produce paired belts of shortening and extension as observed. The well resolved slab beneath the northern Apennines appears to have a lateral edge near latitude $\sim$43°N [*Piromallo and Morelli*, 2003; *Wortel and Spakman*, 2000; *Benoit et al.*, 2011]. This edge has been interpreted as a tear [*Wortel and Spakman*, 2000] or hole [*Lucente et al.*, 1999; *Wortel and Spakman*, 2000; *Piromallo and Morelli*, 2003] in the slab. However, the slab tear model may not fit the observed pattern of vertical rates, which shows no appreciable variation along strike within our study region. Whether the differential vertical motions expected from slab tearing would be large enough to be detected geodetically is an open question. The short wavelength of vertical deformation observed in the GPS data of the order of 10s km likely requires a shallow (crustal) level source.

7. Conclusions

[55] We have estimated crustal motions in northern Italy using a large set of available GPS data to investigate the relationships between crustal kinematics and mantle structure. The crustal velocities that we obtain are consistent with previous studies of crustal motion, but the number of stations and quantity of data that we use provides significantly

improved resolution of the northern Apennines strain rate field relative to previous studies. Present-day crustal motions reveal a wide belt of extension within and to the southwest of the orogen, a narrow belt of shortening located along the northern Apennines range front, and divergent motion between the Northern Adria microplate and the Eurasia plate across the northern Apennines orogen. The pattern of extension and shortening is inconsistent with models that appeal exclusively to either post-orogenic extension driven by excess crustal buoyancy, or to upper plate retreat, although these processes may contribute to the modern deformation field at some level. The observed pattern of deformation seems most consistent with dynamic models appealing to excess mantle buoyancy in the wake of a sinking slab and/or lateral changes in horizontal compressive stress or basal tractions associated with slab rollback. However, models that appeal exclusively to slab sinking do not account for the net divergence across the range. Therefore, we suggest that the modern crustal velocity field is the surface manifestation of both a sinking northern Apennines slab and a retreating upper plate. Slab sinking could represent rollback of an actively subducting slab, albeit at slow rates, or passive delamination of Adria mantle lithosphere. Upper plate retreat could be driven by small-scale circulation in the Mediterranean, by differential motion of Adria and Eurasia with respect to the mesosphere, or by excess gravitational potential energy deriving form upwelling mantle in the wake of the sinking slab. Further geodynamic modeling constrained by the crustal kinematics discussed here could potentially shed light on the relative contributions of these processes.

[56] **Acknowledgments.** The RETREAT GPS experiment was funded by NSF Continental Dynamics grants EAR-0447117 and EAR-0538036, with additional support provided by Instituto Nazionale di Geofisica e Volcanologia (INGV). Equipment and field engineer support were provided by UNAVCO, the University of Bologna (Paolo Baldi and Massimo Bacchetti), and INGV (Sergio Del Mese, Angelo Massucci, Luciano Giovani, Elisabetta D'Anstasio, Sergio Mantenuto, Nicola D'Agostino, and Giulio Selvaggi). We thank Ryan Bierma, Luca Caricchi, Jim Normandeau, Rocco Malservisi, Frank Pazzaglia, and Karl Wegmann for help in the field. Some of the GPS data were collected with assistance from the UNAVCO Facility. Two anonymous reviewers provided constructive comments that helped to improve this manuscript.

References

Altamimi, Z., X. Collilieux, J. Legrand, B. Garayt, and C. Boucher (2007), ITRF2005: A new release of the International Terrestrial Reference Frame based on time series of station positions and earth orientation parameters, *J. Geophys. Res.*, *112*, B09401, doi:10.1029/2007JB004949.

Anderson, H., and J. Jackson (1987), Active tectonics of the Adriatic region, *Geophys. J. R. Astron. Soc.*, *91*(3), 937–983, doi:10.1111/j.1365-246X.1987.tb01675.x.

Argnani, A., et al. (2003), Gravity tectonics driven by Quaternary uplift in the Northern Apennines: Insights from the La Spezia-Reggio Emilia geo-transect, *Quat. Int.*, *101-102*, 13–26, doi:10.1016/S1040-6182(02)00088-5.

Baldi, P., G. Casula, N. Cenni, F. Loddo, and A. Pesci (2009), GPS-based monitoring of land subsidence in the Po Plain (northern Italy), *Earth Planet. Sci. Lett.*, *288*(1–2), 204–212, doi:10.1016/j.epsl.2009.09.023.

Barani, S., D. Scafidi, and C. Eva (2010), Strain rates in northwestern Italy from spatially smoothed seismicity, *J. Geophys. Res.*, *115*, B07302, doi:10.1029/2009JB006637.

Barba, S., M. M. C. Carafa, and E. Boschi (2008), Experimental evidence for mantle drag in the Mediterranean, *Geophys. Res. Lett.*, *35*, L06302, doi:10.1029/2008GL033281.

Battaglia, M., M. Murray, E. Serpelloni, and R. Bürgmann (2004), The Adriatic region: An independent microplate within the Africa-Eurasia collision zone, *Geophys. Res. Lett.*, *31*, L09605, doi:10.1029/2004GL019723.

Baxter, S. C., S. Kedar, J. W. Parker, F. H. Webb, S. E. Owen, A. Sibthorpe, and D. Dong (2011), Limitations of strain estimation techniques from discrete deformation observations, *Geophys. Res. Lett.*, *38*, L01305, doi:10.1029/2010GL046028.

Benedetti, L., P. Tapponnier, Y. Gaudemer, I. Manighetti, and J. Van der Woerd (2003), Geomorphic evidence for an emergent active thrust along the edge of the Po Plain: The Broni-Stradella fault, *J. Geophys. Res.*, *108*(B5), 2238, doi:10.1029/2001JB001546.

Bennett, R. A. (2008), Instantaneous deformation from continuous GPS: Contributions from quasi-periodic loads, *Geophys. J. Int.*, *174*(3), 1052–1064, doi:10.1111/j.1365-246X.2008.03846.x.

Bennett, R. A., and S. Hreinsdóttir (2007), Constraints on vertical crustal motion for long baselines in the central Mediterranean region using continuous GPS, *Earth Planet. Sci. Lett.*, *257*(3–4), 419–434, doi:10.1016/j.epsl.2007.03.008.

Bennett, R. A., S. Hreinsdóttir, M. Velasco, and N. Fay (2007), GPS constraints on vertical crustal motion in the northern Basin and Range, *Geophys. Res. Lett.*, *34*, L22319, doi:10.1029/2007GL031515.

Benoit, M. H., M. Torpey, K. Liszewski, V. Levin, and J. Park (2011), P and S wave upper mantle seismic velocity structure beneath the northern Apennines: New evidence for the end of subduction, *Geochem. Geophys. Geosyst.*, *12*, Q06004, doi:10.1029/2010GC003428.

Bertotti, G., R. Capozzi, and V. Picotti (1997), Extension controls quaternary tectonics, geomorphology and sedimentation of the N-Appennies foothills and adjacent Po Plain (Italy), *Tectonophysics*, *282*(1–4), 291–301, doi:10.1016/S0040-1951(97)00229-1.

Bianchi, I., J. Park, N. Piana Agostinetti, and V. Levin (2010), Mapping seismic anisotropy using harmonic decomposition of receiver functions: An application to Northern Apennines, Italy, *J. Geophys. Res.*, *115*, B12317, doi:10.1029/2009JB007061.

Blewitt, G., and D. Lavallée (2002), Effect of annual signals on geodetic velocity, *J. Geophys. Res.*, *107*(B7), 2145, doi:10.1029/2001JB000570.

Bourne, S., P. England, and B. Parsons (1998), The motion of crustal blocks driven by flow of the lower lithosphere and implications for slip rates of continental strike-slip faults, *Nature*, *391*(6668), 655–659, doi:10.1038/35556.

Buble, G., Bennett, R. A., and S. Hreinsdóttir (2010), Tide gauge and GPS measurements of crustal motion and sea level rise along the eastern margin of Adria, *J. Geophys. Res.*, *115*, B02404, doi:10.1029/2008JB006155.

Calais, E., J. Nocquet, F. Jouanne, and M. Tardy (2002), Current strain regime in the Western Alps from continuous Global Positioning System measurements, 1996–2001, *Geology*, *30*(7), 651–654, doi:10.1130/0091-7613(2002)030<0651:CSRITW>2.0.CO;2.

Calderoni, G., R. Di Giovambattista, and P. Burrato (2009), A seismic sequence from northern Apennines (Italy) provides new insight on the role of fluids in the active tectonics of accretionary wedges, *Earth Planet. Sci. Lett.*, *281*(1–2), 99–109, doi:10.1016/j.epsl.2009.02.015.

Carmignani, L., and R. Kligfield (1990), Crustal extension in the northern Apennines: The transition from compression to extension in the Alpi Apuane core complex, *Tectonics*, *9*(6), 1275–1303, doi:10.1029/TC009i006p01275.

Carminati, E., M. Wortel, W. Spakman, and R. Sabadini (1998), The role of slab detachment processes in the opening of the western-central Mediterranean basins: Some geological and geophysical evidence, *Earth Planet. Sci. Lett.*, *160*(3–4), 651–665, doi:10.1016/S0012-821X(98)00118-6.

Carminati, E., G. Martinelli, and P. Severi (2003a), Influence of glacial cycles and tectonics on natural subsidence in the Po Plain (northern Italy): Insights from ^{14}C ages, *Geochem. Geophys. Geosyst.*, *4*(10), 1082, doi:10.1029/2002GC000481.

Carminati, E., C. Doglioni, and D. Scrocca (2003b), Apennines subduction-related subsidence of Venice (Italy), *Geophys. Res. Lett.*, *30*(13), 1717, doi:10.1029/2003GL017001.

Cavaliere, A., E. Serpelloni, and M. Bacchetti (2010), La rete GPS del progetto RETREAT, *Tech. Rep. 136*, Ist. Naz. di Geofis. e Vulcanol., Rome. [Available at http://portale.ingv.it/portale_ingv/portale_ingv/produzione-scientifica/rapporti-tecnici-ingv/archivio/copy_of_numeri-pubblicati-2010/2010-03-29.0362418444.]

Collettini, C., A. Niemeijer, C. Viti, and C. Marone (2009), Fault zone fabric and fault weakness, *Nature*, *462*, 907–910, doi:10.1038/nature08585.

D'Agostino, N., R. Giuliani, M. Mattone, and L. Bonci (2001), Active crustal extension in the central Apennines (Italy) inferred from GPS measurements in the interval 1994–1999, *Geophys. Res. Lett.*, *28*(10), 2121–2124, doi:10.1029/2000GL012462.

D'Agostino, N., D. Cheloni, S. Mantenuto, G. Selvaggi, A. Michelini, and D. Zuliani (2005), Strain accumulation in the southern Alps (NE Italy) and deformation at the northeastern boundary of Adria observed by CGPS measurements, *Geophys. Res. Lett.*, *32*, L19306, doi:10.1029/2005GL024266.

D'Agostino, N., A. Avallone, D. Cheloni, E. D'Anastasio, S. Mantenuto, and G. Selvaggi (2008), Active tectonics of the Adriatic region from

GPS and earthquake slip vectors, *J. Geophys. Res.*, *113*, B12413, doi:10.1029/2008JB005860.

D'Agostino, N., S. Mantenuto, and E. D'Anastasio (2009), Contemporary crustal extension in the Umbria-Marche Apennines from regional CGPS networks and comparison between geodetic and seismic deformation, *Tectonophysics*, *476*, 3–12, doi:10.1016/j.tecto.2008.09.033.

Dalmayrac, B., and P. Molnar (1981), Parallel thrust and normal faulting in Peru and constraints on the state of stress, *Earth Planet. Sci. Lett.*, *55*, 473–481, doi:10.1016/0012-821X(81)90174-6.

DeMets, C., R. G. Gordon, and D. Argus (2010), Geologically current plate motions, *Geophys. J. Int.*, *181*, 1–80, doi:10.1111/j.1365-246X.2009.04491.x.

Di Bucci, D., and S. Mazzoli (2002), Active tectonics of the northern Apennines and Adria geodynamics: New data and a discussion, *J. Geodyn.*, *34*(5), 687–707, doi:10.1016/S0264-3707(02)00107-2.

Doglioni, C. (1990), The global tectonic pattern, *J. Geodyn.*, *12*(1), 21–38, doi:10.1016/0264-3707(90)90022-M.

Doglioni, C. (1991), A proposal for the kinematic modelling of W-dipping subductions: Possible applications to the Tyrrhenian-Apennines system, *Terra Nova*, *3*(4), 423–434, doi:10.1111/j.1365-3121.1991.tb00172.x.

Dong, D., T. Herring, and R. King (1998), Estimating regional deformation from a combination of space and terrestrial geodetic data, *J. Geod.*, *72*(4), 200–214, doi:10.1007/s001900050161.

Faccenda, M., G. Minelli, and T. V. Gerya (2009), Coupled and decoupled regimes of continental collision: Numerical modeling, *Earth Planet. Sci. Lett.*, *278*, 337–349, doi:10.1016/j.epsl.2008.12.021.

Fellin, M. G., P. W. Reiners, M. T. Brandon, E. Wüthrich, M. L. Balestrieri, and G. Molli (2007), Thermochronologic evidence for the exhumational history of the Alpi Apuane metamorphic core complex, northern Apennines, Italy, *Tectonics*, *26*, TC6015, doi:10.1029/2006TC002085.

de Ferrari, R., G. Ferretti, S. Barani, and D. Spallarossa (2010), Investigating on the 1920 Garfagnana earthquake (Mw=6.5); Evidences of site effects in Villa Collemandina (Tuscany, Italy), *Soil Dyn. Earthquake Eng.*, *30*(12), 1417–1429, doi:10.1016/j.soildyn.2010.07.004.

Forsyth, D. W. (1992), Finite extension and low angle normal faulting, *Geology*, *20*, 27–30, doi:10.1130/0091-7613(1992)020<0027:FEALAN>2.3.CO;2.

Galadini, F., and P. Messina (2004), Early Middle Pleistocene eastward migration of the Abruzzi Apennine (central Italy) extensional domain, *J. Geodyn.*, *37*(1), 57–81, doi:10.1016/j.jog.2003.10.002.

Galadini, F., C. Meletti, and E. Vittori (2001), Major active faults in Italy: Available surficial data, *Neth. J. Geosci.*, *80*, 273–296.

Galli, P., F. Galadini, and D. Pantosti (2008), Twenty years of paleoseismology in Italy, *Earth Sci. Rev.*, *88*(1–2), 89–117, doi:10.1016/j.earscirev.2008.01.001.

Gogus, O. H., and R. N. Pysklywec (2008), Near-surface diagnostics of dripping or delaminating lithosphere, *J. Geophys. Res.*, *113*, B11404, doi:10.1029/2007JB005123.

Gvirtzman, Z., and A. Nur (2001), Residual topography, lithospheric structure and sunken slabs in the central Mediterranean, *Earth Planet. Sci. Lett.*, *187*(1–2), 117–130, doi:10.1016/S0012-821X(01)00272-2.

Herring, T., R. King, and S. McClusky (2010a), GAMIT Reference Manual, Release 10.4, report, pp. 1–171, Mass. Inst. of Technol., Cambridge.

Herring, T., R. King, and S. McClusky (2010b), GLOBK Reference Manual: Global Kalman filter VLBI and GPS analysis program, Release 10.4, report, 1–95, Mass. Inst. of Technol., Cambridge.

Hill, E. M., J. L. Davis, M. E. Tamisiea, and M. Lidberg (2010), Combination of geodetic observations and models for glacial isostatic adjustment fields in Fennoscandia, *J. Geophys. Res.*, *115*, B07403, doi:10.1029/2009JB006967.

Hreinsdóttir, S., and R. A. Bennett (2009), Active aseismic creep on the Alto Tiberina low-angle normal fault, Italy, *Geology*, *37*(8), 683–686, doi:10.1130/G30194A.1.

Jolivet, L., et al. (1998), Midcrustal shear zones in postorogenic extension: Example from the northern Tyrrhenian Sea, *J. Geophys. Res.*, *103*(B6), 12,123–12,160, doi:10.1029/97JB03616.

Kreemer, C., W. E. Holt, and A. J. Haines (2003), An integrated global model of present-day plate motions and plate boundary deformation, *Geophys. J. Int.*, *154*, 8–34, doi:10.1046/j.1365-246X.2003.01917.x.

Lamb, S. (1994), Behavior of the brittle crust in wide plate boundary zones, *J. Geophys. Res.*, *99*, 4457–4483.

Langbein, J. (2008), Noise in GPS displacement measurements from Southern California and Southern Nevada, *J. Geophys. Res.*, *113*, B05405, doi:10.1029/2007JB005247.

Larson, K., and F. Webb (1991), Application of the Global Positioning System to crustal deformation measurement 2. The influence of errors in orbit determination networks, *J. Geophys. Res.*, *96*, 16,567–16,584, doi:10.1029/91JB01276.

Levin, V., L. Margheriti, J. Park, and A. Amato (2002), Anisotropic seismic structure of the lithosphere beneath the Adriatic coast of Italy constrained with mode-converted body waves, *Geophys. Res. Lett.*, *29*(22), 2058, doi:10.1029/2002GL015438.

Lucente, F., C. Chiarabba, G. Cimini, and D. Giardini (1999), Tomographic constraints on the geodynamic evolution of the Italian region, *J. Geophys. Res.*, *104*(B9), 20,307–20,327, doi:10.1029/1999JB900147.

Malinverno, A., and W. Ryan (1986), Extension in the Tyrrhenian Sea and shortening in the Apennines as result of arc migration driven by sinking of the lithosphere, *Tectonics*, *5*(2), 227–245, doi:10.1029/TC005i002p00227.

Montone, P., and M. Mariucci (1999), Active stress along the NE external margin of the Apennines: The Ferrara arc, northern Italy, *J. Geodyn.*, *28*(2–3), 251–265, doi:10.1016/S0264-3707(98)00041-6.

Nur, A., and G. Mavko (1974), Postseismic viscoelastic rebound, *Science*, *183*(4121), 204–206, doi:10.1126/science.183.4121.204.

Panza, G., R. Raykova, E. Carminati, and C. Doglioni (2007), Upper mantle flow in the western Mediterranean, *Earth Planet. Sci. Lett.*, *257*(1–2), 200–214, doi:10.1016/j.epsl.2007.02.032.

Pialli, G., and W. Alvarez (1995), Tectonic setting of the Miocene Northern Apennines: The problem of contemporaneous compression and extension, in *Miocene Stratigraphy: An Integrated Approach*, edited by A. Montanari, G. S. Odin, and R. Coccioni, *Dev. Palaeontol. Stratigr.*, *15*, 167–185, doi:10.1016/S0920-5446(06)80016-6.

Piccinini, D., C. Chiarabba, and P. Augliera (2006), Compression along the northern Apennines? Evidence from the Mw 5.3 Monghidoro earthquake, *Terra Nova*, *18*(2), 89–94, doi:10.1111/j.1365-3121.2005.00667.x.

Picotti, V., and F. Pazzaglia (2008), A new active tectonic model for the construction of the northern Apennines mountain front near Bologna (Italy), *J. Geophys. Res.*, *113*, B08412, doi:10.1029/2007JB005307.

Piromallo, C., and A. Morelli (2003), P wave tomography of the mantle under the Alpine-Mediterranean area, *J. Geophys. Res.*, *108*(B2), 2065, doi:10.1029/2002JB001757.

Platt, J. (1986), Dynamics of orogenic wedges and the uplift of high-pressure metamorphic rocks, *Bull. Geol. Soc. Am.*, *97*(9), 1037–1053, doi:10.1130/0016-7606(1986)97<1037:DOOWAT>2.0.CO;2.

Pondrelli, S., G. Ekström, and A. Morelli (2001), Seismotectonic re-evaluation of the 1976 Friuli, Italy, seismic sequence, *J. Seismol.*, *5*(1), 73–83, doi:10.1023/A:1009822018837.

Pondrelli, S., S. Salimbenia, G. Ekström, A. Morellia, P. Gasperinic, and G. Vannuccia (2006), The Italian CMT dataset from 1977 to the present, *Phys. Earth Planet. Inter.*, *159*, 286–303, doi:10.1016/j.pepi.2006.07.008.

Rosenbaum, G., and G. Lister (2004), Neogene and Quaternary rollback evolution of the Tyrrhenian Sea, the Apennines, and the Sicilian Maghrebides, *Tectonics*, *23*, TC1013, doi:10.1029/2003TC001518.

Royden, L. (1993), The tectonic expression of slab pull at continental convergent boundaries, *Tectonics*, *12*, 303–325, doi:10.1029/92TC02248.

Savage, J., and W. Prescott (1978), Asthenosphere readjustment and earthquake cycle, *J. Geophys. Res.*, *83*, 3369–3376, doi:10.1029/JB083iB07p03369.

Segall, P. (2010), *Earthquake and Volcano Deformation*, 432 pp., Princeton Univ. Press, Princeton, N. J.

Selvaggi, G., et al. (2001), The Mw 5.4 Reggio Emilia 1996 earthquake: Active compressional tectonics in the Po Plain, Italy, *Geophys. J. Int.*, *144*(1), 1–13, doi:10.1046/j.0956-540X.2000.01255.x.

Serpelloni, E., M. Anzidei, P. Baldi, G. Casula, and A. Galvani (2005), Crustal velocity and strain-rate fields in Italy and surrounding regions: New results from the analysis of permanent and non-permanent GPS networks, *Geophys. J. Int.*, *161*(3), 861–880, doi:10.1111/j.1365-246X.2005.02618.x.

Serpelloni, E., M. Anzidei, P. Baldi, G. Casula, and A. Galvani (2006), GPS measurement of active strains across the Apennines, *Ann. Geophys.*, *49*(1), 319–329.

Shen, Z., D. Jackson, and B. Ge (1996), Crustal deformation across and beyond the Los Angeles basin from geodetic measurements, *J. Geophys. Res.*, *101*(B12), 27,957–27,980, doi:10.1029/96JB02544.

Shen, Z., D. Jackson, and Y. Kagan (2007), Implications of geodetic strain rate for future earthquakes, with a five-year forecast of M5 earthquakes in southern California, *Seismol. Res.*, *78*, 116–120, doi:10.1785/gssrl.78.1.116.

Spinler, J. C., R. A. Bennett, M. L. Anderson, S. F. McGill, S. Hreinsdóttir, and A. McCallister (2010), Present-day strain accumulation and slip rates associated with southern San Andreas and eastern California shear zone faults, *J. Geophys. Res.*, *115*, B11407, doi:10.1029/2010JB007424.

Stein, S., and G. Sella (2006), Pleistocene change from convergence to extension in the Apennines as a consequence of Adria microplate motion, in *The Adria Microplate: GPS Geodesy, Tectonics and Hazards*, pp. 21–34, Springer, New York.

Stocchi, P., G. Spada, and S. Cianetti (2005), Isostatic rebound following the Alpine deglaciation: Impact on the sea level variations and vertical

movements in the Mediterranean region, *Geophys. J. Int.*, *162*(1), 137–147, doi:10.1111/j.1365-246X.2005.02653.x.
Sun, W., and S. Okubo (2002), Effects of earth's spherical curvature and radial heterogeneity in dislocation studies—for a point dislocation, *Geophys. Res. Lett.*, *29*(12), 1605, doi:10.1029/2001GL014497.
Thatcher, W., and J. Rundle (1979), Model for the earthquake cycle in underthrust zones, *J. Geophys. Res.*, *84*, 5540–5556, doi:10.1029/JB084iB10p05540.
Thomson, S. N., M. T. Brandon, P. W. Reiners, M. Zattin, P. J. Isaacson, and M. L. Balestrieri (2009), Thermochronologic evidence for orogen-parallel variation in wedge kinematics during extending convergent orogenesis of the northern Apennines Italy, *Geol. Soc. Am. Bull.*, *122*, 1160–1179.
Velasco, M. S., R. A. Bennett, R. A. Johnson, and S. Hreinsdóttir (2010), Subsurface fault geometries and crustal extension in the eastern Basin and Range Province, western U.S, *Tectonophysics*, *488*(1–4), 131–142, doi:10.1016/j.tecto.2009.05.010.
Waschbusch, P., and C. Beaumont (1996), Effect of a retreating subduction zone on deformation in simple regions of plate convergence, *J. Geophys. Res.*, *101*, 28,133–28,148.
Wdowinski, S., Y. Bock, J. Zhang, P. Fang, and J. Genrich (1997), Southern California permanent GPS geodetic array: Spatial filtering of daily positions for estimating coseismic and postseismic displacements induced by the 1992 Landers earthquake, *J. Geophys. Res.*, *102*(B8), 18,057–18,070.
Weber, J., M. Vrabec, P. Pavlovcic-Preseren, T. Dixon, Y. Jiang, and B. Stopar (2010), GPS-derived motion of the Adriatic microplate from Istria Peninsula and Po Plain sites, and geodynamic implications, *Tectonophysics*, *483*, 214–222, doi:10.1016/j.tecto.2009.09.001.
Wortel, M., and W. Spakman (2000), Subduction and slab detachment in the Mediterranean-Carpathian region, *Science*, *290*(5498), 1910–1917, doi:10.1126/science.290.5498.1910.

M. Anzidei, Istituto Nazionale di Geofisica e Vulcanologia, Centro Nazionale Terremoti, Via di Vigna Murata 605, I-00143 Rome, Italy.

T. Basic, Faculty of Geodesy, University of Zagreb, Zagreb 10144, Croatia.

R. A. Bennett, G. Buble, and S. Hreinsdóttir, Department of Geosciences, University of Arizona, Tucson, AZ 85721-0077, USA.

M. T. Brandon, Department of Geology and Geophysics, Yale University, New Haven, CT 06511, USA.

G. Casale, Department of Earth and Space Sciences, University of Washington, PO Box 351310, Seattle, WA 98195-1310, USA.

A. Cavaliere and E. Serpelloni, Istituto Nazionale di Geofisica e Vulcanologia, Sezione di Bologna, Via D. Creti 12, I-40128 Bologna, Italy.

M. Marjonovic, Croatian State Geodetic Administration, Gruška 20, Zagreb 10000, Croatia.

G. Minelli, Dipartimento di Scienze della Terra, Universitá di Perugia, Piazza dell'Universitá 1, I-06100 Perugia, Italy.

G. Molli, Dipartimento di Scienze della Terra, Universita` di Pisa, Via S. Maria 53, I - 56126 Pisa, Italy.

A. Montanari, Osservatorio Geologico di Coldigioco, I-62020 Frontale di Apiro, Italy.